Fall 12-2021

Fabrication & Mechanical Properties of Hastelloy-X Matrix Ceramic Composite

Sultan Stewart
Embry-Riddle Aeronautical University, stewas23@my.erau.edu

FABRICATION & MECHANICAL PROPERTIES OF HASTELLOY-X MATRIX CERAMIC COMPOSITE

By

Sultan Stewart

A Thesis Submitted to the Faculty of Embry-Riddle Aeronautical University

in Partial Fulfillment of the Requirements for the Degree of

Master of Science in Aerospace Engineering

December 2021

Embry-Riddle Aeronautical University

Daytona Beach, Florida

FABRICATION & MECHANICAL PROPERTIES OF HASTELLOY-X MATRIX CERAMIC COMPOSITE

By

Sultan Stewart

This Thesis was prepared under the direction of the candidate's Thesis Committee Chair, Dr. Sirish Namilae, Department of Aerospace Engineering, and has been approved by the members of the Thesis Committee. It was submitted to the Office of the Senior Vice President for Academic Affairs and Provost, and was accepted in the partial fulfillment of the requirements for the Degree of Master of Science in Aerospace Engineering.

THESIS COMMITTEE

Sirish Namilae — Digitally signed by Sirish Namilae Date: 2021.12.08 14:37:26 -05'00'

Chairman, Dr. Sirish Namilae

Marwan Al-Haik — Digitally signed by Marwan Al-Haik Date: 2021.12.09 10:56:16 -05'00'

Member, Dr. Marwan Al-Haik

David J. Sypeck — Digitally signed by David J. Sypeck Date: 2021.12.10 10:40:49 -05'00'

Member, Dr. David Sypeck

Daewon Kim — Digitally signed by Daewon Kim Date: 2021.12.10 11:59:35 -05'00'

Graduate Program Coordinator, Dr. Daewon Kim

Date

James W. Gregory — Digitally signed by James W. Gregory Date: 2021.12.10 14:33:02 -05'00'

Dean of the College of Engineering, Dr. James W. Gregory

Date

Associate Provost of Academic Support, Dr. Christopher Grant

Date

ACKNOWLEDGEMENTS

I would like to take this opportunity to thank all those who encouraged, supported, and helped me in completing this thesis. A sincere thank you to my advisor, Dr. Sirish Namilae, who's guidance, knowledge and patience was more than I could ask for throughout this process. I would also like to thank my committee members, Dr. Marwan S. Al-Haik and Dr. David J. Sypeck for their feedback and counsel in developing this thesis.

A special thanks to Samarth Motagi for teaching me the wet layer process, Sandeep Chava for his lessons on operating the x-ray tomograph, and Suma Ayyagari for performing the nanoindentation test using the nanoindenter procured through NSF MRI award 2018375.

I must also thank my employer, Technetics Group in Deland, FL for providing the samples and furnace needed for experimentation. My boss, Bob Schricker for being flexible in my work schedule to allow me to complete certain time sensitive task. My coworker Kelly Ceiler whose knowledge of the manufacturing process was extremely helpful. Also, my fellow coworker Elaine Motyka whose expertise in materials and general knowledge was highly appreciated throughout this entire process.

Lastly, I want to thank my wife for her constant love, support and encouragement through the late nights and long weekends. Her belief in me has been unwavering and I appreciate it more than I can put into words.

ABSTRACT

In the aerospace industry, there is a desire for increased thermal and mechanical properties of sealing materials. In this thesis, porous Hastelloy-X alloy scaffolds with 80% porosity, currently used for fabricating seals in turbine applications, were used as the base material. The microstructure of the porous Hastelloy-X scaffolds was infiltrated using a room temperature curing silicate colloid (trade name -Dichtol HTWG Hydro #2506) and a novel zirconia based colloid to fabricate the metal matrix composites. Various fabrication processes, some using vacuum and pressure to assist the flow were utilized to infiltrate the scaffolds. The green composites were then cured at the required room or elevated temperature. Composites were characterized using x-ray tomography and scanning electron microscopy (SEM) imaging to analyze the pore infiltration. Rockwell hardness and nanoindentation were measured to determine changes in material properties.

Through porosity calculations and SEM imaging, it was determined that vacuum was required for the most effective infiltration. The silicate colloid required a method of drawing the colloid through the scaffold while traditional vacuum was sufficient for the zirconia colloid. Hardness results were influenced by the infiltration method, the method requiring the vacuum to draw the colloid through the scaffold had the greatest increase in hardness. Despite porosity levels, the zirconia composite hardness exceeded the silicate composite at both the Rockwell and nano scale. The mechanism for decrease in plasticity and increase in hardness are examined. The silicate and zirconia composites show better material performance in some areas however, further testing is needed to determine if they are suitable substitutes for the current Hastelloy-X scaffold as a turbine seal.

TABLE OF CONTENTS

LIST OF FIGURES

Figure Page

Figure Page

LIST OF TABLES

NOMENCLATURE

V_1 = volume of ethanol

V_2 = volume of ethanol and the submerged scaffold

V_3 = volume of ethanol once the scaffold is removed

V_g = volume of scaffold material

V_a = apparent scaffold volume

h_f = final indentation depth after complete unloading

B and m = fitting parameters

m = fitting parameters

S = contact stiffness

h_c = contact depth

A_c = contact area

R = radius of the indenter tip

β = correction factor

V_s = Poisson's ratio of the specimen

E_i = elastic modulus of the indenter

V_i = Poisson's ratio of the indenter

E_i = Indenter's elastic modulus

E_{op} = indentation modulus equation

1. Introduction

Applications that require sealing to protect internal rotating components and provide optimum working conditions are critical in turbine applications. To minimize the required clearance for rotating turbine blade tips and interstage labyrinth seal knife edges an abradable material is often used ("Feltmetal ™ Abradable Seals," n.d.). As technology continues to develop there is an increased need for these sealing material properties to improve and preform at higher temperatures. Porous Hastelloy-X is one of the materials used for this application currently. To achieve a higher level of performance, adding ceramic to this sealing materials is a viable option. The high melting point and resistance to chemical degradation, creep, oxidation, thermal shock, decomposition and softening makes ceramics a preferred choice (Lukacs III, 2006).

1.1. Research Questions

The research questions addressed in this thesis are as follows:

1. Typical manufacturing process for the composite requires mixing the powder form of the matrix and the reinforcement materials. Can a composite be manufactured using a porous metal scaffold as a matrix preform?
2. What are the processing considerations for infiltrating and manufacturing metal matrix composites using ceramic colloid for (a) room temperature curing, and (b) high temperature sintering?
3. How do the mechanical properties relevant to seal applications alter for the composite compared to the metal?

1.2. Objective

A desired property of turbine seals is oxidation resistance. The material's performance ability decreases due to high temperature oxidation, sulfidation attack and aqueous corrosion. During oxidation, Hastelloy-X forms a chromium based protective oxide which vaporizes at its rated usage temperature use of ~815°C. Oxide formation increases mass by attaching oxygen atoms to form the chromium nickel oxide, continuingly thinning the metal fibers to do so. This leads to a decrease in strength and ductility of the fibers ("Feltmetal™: Adaptable Abradable Materials," n.d.).

Abradablilty is another important property when dealing with turbine sealing materials. When the blade contacts the seal, it deforms the metal into the pores, increasing the contact area, shear stress, and temperature due to friction. Rub testing conducted on Hastelloy-X samples showed that density had a significant effect on blade wear, determining that densities above 40% (porosity below 60%) reduced the abrasion resistance of the composite ("Feltmetal™: Adaptable Abradable Materials," n.d.).

In balance with abradability, erosion resistance must be considered. Continuous contact with foreign particles will eventually wear the seal, and these particles can eventually make their way into the interior, damaging the components. The natural tortuous path created by the pores aims to minimizes this, but can this be improved for longer seal service life.

The objectives of this thesis are as follows:

1. To develop materials with improved high temperature (>537°C) properties relevant to the seal application. These properties include minimized abrasion resistance to reduce wear on turbine blades and

localized heating, lower air permeability to reduce outside contaminates from entering the engine, and lower oxidation rate to preserve abradable material strength.

2. Investigate fabrication methods for metal matrix composites (MMCs) that satisfy the requirements of the seal application.
3. Microstructural characterization and mechanical testing of fabricated composite specimens.

2. Background

The benefits of metal matrix composites (MMCs) are wide ranging and well documented. Companies and laboratories have been able to tailor traditional composite manufacturing processes to maximize the desired material performance depending on the specific application. It stands to reason that a composite manufacturing process for Hastelloy-X scaffolds in turbines can be developed as well. In this chapter, we introduce background literature on various material components and fabrication methods.

2.1. Hastelloy-X Porous Scaffolds

Figure 2.1 shows a typical abradable seal manufactured by Technetics Group. The backing ring defines the design envelope and has limited space due to design considerations. Any expansion to the material could cause buckling to occur or damage the surrounding engine hardware ("Feltmetal™: Adaptable Abradable Materials," n.d.). The turbine blades interact with the material on the inside of the seal shown in Figure 2.1.

A common seal material currently used in the aerospace industry is a 80% porous Hastelloy-X scaffold. Hastelloy-X is a Ni based material with the alloying elements seen in Table 2-1. The mechanical and thermal properties of the Hastelloy-X material are listed in Table 2-2. It's believed that the combination of high strength and low ductility is ideal for reducing the amount of energy needed for abrasions and the amount of wear experienced by the rotating blade.

The porous metal scaffold is manufactured as follows: Hastelloy-X fibers are cleaned and sifted to remove aggregates then dispersed to create fiber sheets. The sheets are then vacuum sintered to form diffusion bonds between fibers. These sintered sheets are formed to a final porosity ranging from 68% to 86%, and are then rolled, formed, or

machined to customer requirements.

Figure 2.1 Technetics Group Abradable ("Feltmetal ™ Abradable Seals," n.d.)

Table 2.1

Hastelloy-X Composition Details

Composition	**Weight Percent (wt%)**
C (carbon)	0.1
Co (cobalt)	0.5 - 2.5
Cr (chromium)	20.5 - 23.0
Fe (iron)	17.0 - 20.0
Mn (Manganese)	0 - 1.0
Mo (molybdenum)	8.0 - 10.0
Ni (nickel)	41.3 - 53.8
P (phosphorus)	0 - 0.04
S (sulfur)	0 - 0.03
Si (silicon)	0 - 1.0
W (tungsten)	0.2 - 1.0

(ANSYS, 2020)

Table 2.2

Hastelloy-X Mechanical & Thermal Properties

Properties	**Values**
Young's Modulus	205 - 216 GPa
Yield Strength (Elastic Limit)	340 - 450 MPa
Tensile Strength	703 - 777 MPa
Shear Modulus	78 - 82 GPA
Hardness – Vickers	160 - 200 HV
Fracture Toughness	186 - 206 MPa$\sqrt{m}$
Melting Point	1.26 e3 - 1.36 e3 °C
Thermal Conductivity	10.4 - 11.3 W/m°C
Thermal Expansion Coefficient	13.7 - 14.4 μstrain/m°C
Thermal Shock Resistance	115 - 153°C

(ANSYS, 2020)

The random arrangement of fibers and the complex path of porosity aids in minimizing the gas permeability while maintaining a low density. Another benefit of the porous structure is the low thermal conductivity which reduces heat transfer to the metal backing ring, Figure 2.1.

2.1.1. Applications

The scaffold's primary use is in aerospace and industrial turbine applications as a rub tolerant material that is forgiving enough to abrade away when contacted by a high-speed rotating blade without wearing the blade, but resilient enough to withstand high temperature velocity gas and particulate erosion ("Feltmetal ™ Abradable Seals," n.d.). A delicate balance between abrasion resistance and erosion resistance must be obtained which makes seal development difficult given the opposing desired material properties.

The scaffold's function is to minimize engine operating clearance between the blade tip and the casing, part 4 of Figure 2.2, reduce leakage of air flow around the blade,

reduce or eliminate wear on rotating hardware, and improve the overall efficiency as well as the life of the engine. It has also been used by gas turbine manufactures to improve flow path efficiency. The Hastelloy-X porous scaffold is used as the matrix for the composites fabricated in this work. The ceramic filler materials are discussed next.

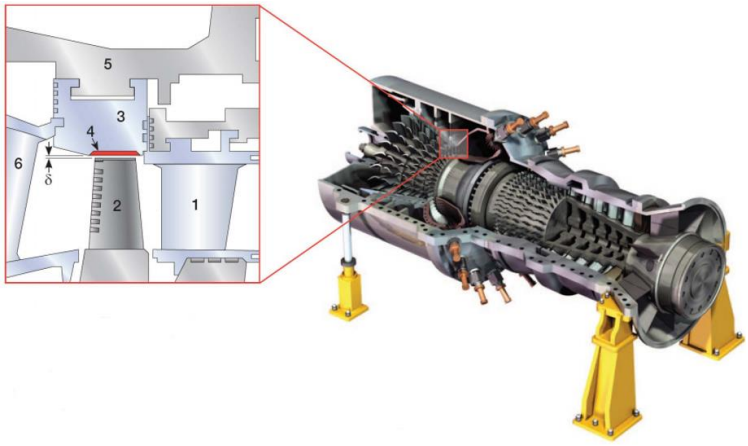

Figure 2.2 Example of Blade Tip Seal Application (Philips et al., 2016, p. 5).

2.2. Ceramic Fillers

2.2.1. Yttria Stabilized Tetragonal Zirconia

Zirconium oxide, commonly referred to as zirconia, is a crystalline oxide which can exists in three phases with different crystal structures. Pure Zirconia exists in monoclinic structure at room temperature. It reversibly changes to the tetragonal structure at 1170°C and cubic structure at 2370°C (Piconi & Maccauro, 1997). During cooling, transition of the tetragonal phase back to monoclinic happens around 970°C. During this phase change a volume expansion of approximately 3-4% occurs, creating stress generated cracks in the zirconia that break into pieces at room temperature. By adding stabilizing oxides,

such as Y_2O_3, to pure zirconia a multiphase material (partially stabilized zirconia) can be generated. The microstructure consists of cubic zirconia as the major phase and monoclinic and tetragonal zirconia precipitates dispersed in the grain boundaries and cubic matrix as the minor phase. The tetragonal precipitates transform to the monoclinic phase when a crack occurs in the material. The stress field created by the crack is opposed by the stress field created by the volume expansion of the phase change from tetragonal to monoclinic. This results in improved strength and toughness Piconi & Maccauro, 1997). This combination of zirconia (ZrO_2) and yttria (Y_2O_3) are what give the oxide its name, yttria stabilized tetragonal zirconia (YSZ) ("Yttria Stabilized Zirconia, YSZ (ZrO2 / Y2O3) Nanoparticles," 2013).

Table 2.3

Yttria Stabilized Tetragonal Zirconia (ANSYS, 2020)

Properties	**Values**
Young's Modulus	97.5 - 103 GPa
Yield Strength (Elastic Limit)	115 - 200 MPa
Tensile Strength	115 - 200 MPa
Shear Modulus	38.3 - 40.1 GPA
Hardness – Vickers	259 - 287 HV
Fracture Toughness	9.52 - 10.5 MPa$\sqrt{m}$
Melting Point	2.55 e3 - 2.7 e3 °C
Thermal Conductivity	1.7 - 2 W/m°C
Thermal Expansion Coefficient	6 - 8.8 μstrain/m°C
Thermal Shock Resistance	151 - 289°C

(ANSYS, 2020)

The mechanical properties of yttria stabilized zirconia (YSZ) used in this work are listed in Table 2-3. YSZ is extremely resistant to crack propagation because of its phase

transformation ability (transformation toughening). When cracks develop, a stress field around the crack also forms. This can cause the tetragonal phase to convert to monoclinic which requires a volume expansion, putting the crack into compression and impeding its growth. The material properties of YSZ include high fracture toughness, hardness, flexural strength, impact resistance, chemical resistance, and erosion resistance which has even made it a practical replacement for metals. Its bending strength and relatively low Young's Modulus give it a more elastic behavior as well (Garvie et al., 1990).

Applications for YSZ include plasma coating, tooth crowning's for its hardness and chemical resistance, a refractory in jet engines, thermal barrier coating in gas turbines, a non-metal material option for knife blades, and jewelry for its hardness and optical properties in the monoclinic form (cubic zirconia). YSZ can act as a electro ceramic because of its ability to conduct ions, this can be used to determine oxygen content in exhaust gases and to measure pH in high temperature water or in fuel cells ("SZ0429 Yttria Stabilized Zirconia," n.d.).

2.2.2. Silicate – Tradename Dichtol

Another filler material used in this work is a silicate based colloid which is marketed with a tradename Dichtol HTWG Hydro (C. Annis, personal communication, October 22, 2020). The silicate colloid is cured at room temperature, resistant to thermal stresses, good chemical stability and corrosion resistance. The application temperature ranges for the primary component silicate varying from -4°C to 704°C. The colloid will carry the resin into the open pores of the scaffold. As the solvent evaporates, the resin is left to fill the open pores. The Hastelloy-X scaffold is non-reactive with silicate or the dispersion agent. The silicate will cure around the Hastelloy-X creating a interlocking

microstructure. Use of silicate based materials as fillers results in a denser microstructure with higher mechanical strength and fracture toughness (Deb et al., 2015). The Dichtol sealant has many variations for low temperature and high temperature applications and has been used in numerous research studies for coating and sealing applications (Zhang & Kong, 2018; Jing & Dejun, 2018, King & Henfling, 2013). The high temperature Dichtol product is commonly used to seal parts that preform in high temperature applications in industry. Specifically, it is used to impregnate castings, and seal parts that have been thermally spray coated or produced using additive manufacturing. Its application applies to a wide range of materials including metal, ceramic, plastic, concrete, wood and textiles ("Dichtol HTWG Hydro Product number", 2018).

2.3. Metal Matrix Composites

MMCs are generally constructed of two phases, the matrix and the reinforcement which is dispersed within the matrix. The matrix phase is a continuous phase that provides base material properties and facilitates load transfer, while the reinforcement provides additional strength, stiffness, wear resistance or other functional properties to the composite. In particulate MMCs, the reinforcement phase is constructed of dispersed particles that block dislocation motion which results in improved material properties such as hardness, thermal conductivity, thermal shock resistance, electrical conductivity etc. (Singh et al., 2017). Commonly used precipitation strengthened alloys experience a decrease in creep resistance at elevated temperatures. This is because particles begin to coarsen and particle size increases. MMCs with a higher volume fraction of a ceramic reinforcements have reduced inter particle spacing. The ceramic particles also have little to no solubility in the MMC, they are inert and therefore do not coarsen. It is because of

these factors that the ceramic reinforced MMCs do not experience a loss of creep resistance at elevated temperatures (Raj, 2018). These material properties are dependent on the amount of reinforcement, how well it's distributed throughout the matrix and which processing method is used to construct the matrix.

2.4. Processing Techniques

MMCs are manufactured using numerous methods including powder consolidation (Haghighi et al., 2012), hot isotactic pressing (Almotairy et al., 2020), diffusion bonding (Lee et al., 1999), physical vapor deposition (Saxena et al., 2017), spray forming (Singer, 1991), electroplating (Bostani et al., 2016), infiltration (Dmitruk et al., 2018), and additive manufacturing approaches (Hehr et al., 2019). This section briefly describes the processing techniques that are most relevant for the methods used in this thesis.

2.4.1. Powder Processing

The general processing of MMCs can be broken down into three steps: preparation of the aqueous solution, creation of green compact and sintering. During creation of the aqueous solution, the metal and ceramic powder is mixed using a dispersion media such as water, a dispersant is added to aid in a homogenous distribution. To improve sintering and reduce heterogeneity throughout the mixing, a particle size of less than 1 nm is suggested.

To break apart any agglomerates or clusters in the suspension a process such as sonification is used followed by ball milling. This is important as agglomerates are inhomogeneous collections in the suspension, there size increases as they encounter other agglomerates throughout the suspension which can create imperfections during sintering. (Bergstrom, 2001). In some cases, after the initial ball milling, a binder is added to the

suspension and additional ball milling performed. This mixing process will reduce the viscosity of the suspension to make formation of the green compacts easier.

Green compacts are created by processes such as slip casting, tape casting, pressure casting, injection molding, etc. The green compacts must then be dried before sintering. If not performed properly, cracks can form during sintering due to large volumes of gas being released in a short time. A proper compact will have a high uniform packing fraction of particles, small and narrow pore size, and a high degree of homogeneity (Bergstrom, 2001). Lastly the green compacts are sintered, the appropriate temperatures, dwell times, ramp up and ramp down rates are dependent on what materials the MMC is constructed of and the environment it will be used in.

2.4.2. Melt Infiltration

There is limited research into infiltration of previously constructed metal scaffolds. But the methods that were found used a process called melt infiltration (Sofianos et al., 2017, 2018; Mattern et al., 2004). In this process, a powder consisting of hydrides such as $NaAlH_4$ or $NaMgH_3$ are ball milled, compressed into pellets, and sintered under dynamic vacuum. The sintering temperature is low enough not to compact the material but high enough to remove the Na and H_2. This leaves behind a porous Aluminum or Magnesium scaffold in the shape of the original pellet. Eutectic mixtures such as lithium borohydride, sodium borohydride or Magnesium borohydride are prepared by ball milling and are melt-infiltrated into the porous scaffold. This is done by heating the scaffold and eutectic mixture to the necessary temperature to melt the eutectic mixture but not the scaffold. The eutectic mixture enters the pores of the scaffold using capillary forces or back pressure.

The results have been successful, with all pores being infiltrated creating a solid pellet. The is mainly due to the larger number of macropores measured in the scaffold pre infiltration and the open interconnective network of pores which is a result of the scaffold manufacturing process (Sofianos et al., 2017, 2018; Mattern et al., 2004).

2.4.3. Selective Laser Melting

Selective laser melting (SLM) is a powder based additive manufacturing process. Like the previous processing techniques, the metal ceramic powders must first be thoroughly mixed to achieve a homogenous mixture, typically using a ball mill. A computer generated 3D model of the part is created and mathematically sliced into thin layers, these layers are imputed into the laser.

Before the SLM processing, a substrate is attached to the building platform and precisely leveled to avoid mistakes in the build procedure. During SLM, a thin layer of powder identical to the sliced layer thickness is deposited on the build platform. The powder is scanned and melted based on the computer program. After the first layer the process is repeated until all layers are complete. By manufacturing layer by layer a porous scaffold can be created. Samples are manufactured in a sealed vacuum chamber filled with argon to minimize oxidation during the process. The processing parameters such as laser power, scan speed, hatch spacing, scanning pattern, powder layer thickness, and beam spot diameter are determined based on the desired final quality of the part (Prashanth et al., 2016).

The benefit of SLM is its high degree of freedom, making it ideal for complex shapes and structures that would be difficult to manufacture using traditional methods. The process is also believed to be less time consuming for complex parts, maximizes material

use, and is more environmentally friendly (Prashanth et al., 2016).

2.5. Characterization and Testing of MMCs

To analyze the microstructure of composites the most common methods for observation are optical microscopes and scanning electron microscopes (SEMs). These are the most common approaches for investigating the dispersion of the reinforcement within the microstructure (Deb et al., 2015; Dourandish et al., 2008; Gonzalo-Juan et al., 2010). In conjunction with these methods, x-ray diffraction is sometimes used for phase determination (Pandey et al., 2018). The most common composite material properties measured are hardness and abrasive resistance. Abrasive resistance is measured by wear test, the sample is fixed and a interchangeable blade is attached to a rotating wheel. The rpm and incursion rate are determined based on the sample and application (Stringer & Marshall , 2012; Feltmetal^{TM}: Adaptable Abradable Materials," n.d.). In addition to these properties, tensile strength, compressive strength, and corrosion resistance are tested using ASTM standard E8/E8M (tensile), E9 (compressive) G31 (corrosion).

2.6. Applications of Metal Matrix Composites

The use of ceramic reinforced MMCs is not uncommon and there are many applications that have already benefited from these composites. In the automotive industry the first major MMC application was for reinforced pistons for Toyota diesel engines in 1983. Toyota's success encouraged Honda to start using MMCs in engine cylinder bores in 1990. Brake components such as discs, rotors, pads and calipers have been manufactured using Al-Mg alloys with Al_2O_3 reinforcements or Al-Si alloys with SiC particulates. The MMC material benefits of higher thermal conductivity, increased wear resistance, reduced braking noise, and low density are desirable in the application.

Drive shafts that previously required two pieces and a center support can now be manufactured as a single piece. The higher specific stiffness of MMCs relative to steel or aluminum has allowed longer length driveshafts to be produced without increasing the diameter. New applications using MMCs also include Toyota's use of powder metallurgy Ti alloys reinforced with TiB particulates for intake and exhaust valves (Miracle, 2005).

The MMC Al/SiC is commonly used in applications requiring thermal management for its lower weight but other factors also make it desirable in this area. Its largest market is in the radio frequency microwave packaging system for telecommunication and radar applications. By integrating the electrical feed through connectors and bonding to the ceramic base in one operation companies have saved a significant amount of money. Another market for thermal management is for microprocessors. Al/SiC is used as heat sinks for integrated circuits packages, printed circuit board cores, cold plates, chip carriers, and heat spreaders. Lastly, MMCs have a high presence as substrates for high power devices. This includes power semiconductor module baseplates which are used in electric motor controllers and as power conversion for cell phone ground station transmitting towers (Miracle, 2005).

In the Aerospace industry MMCs are attractive for their light weight and high strength. Many aerospace parts can be substituted or redesigned for MMCs. Impellers, disks, rotors, shafts, fan and compressor blades, spacers, ducts, frames, links and exhaust structures can all be replaced with a Ti MMC. This would reduce weight by 15 to 50%, while increasing strength and stiffness. Widespread implementation has faced challenges due to the limited demand by suppliers and end users needed to yield a affordable Ti MMC (Singerman & Jackson, 1996).

Space applications have also benefitted from MMCs. The space shuttle orbiter frame and rib truss members in the mid fuel section and the landing gear drag link used B/Al tubular struts. The was determined to be a 45% weight savings when compared to the aluminum design. The high-antenna boom for the Hubble space telescope was made from a graphite/Al composite. The increase stiffness and low coefficient of thermal expansion allowed the boom to maintain its position during space maneuvers. Also, the composite's electrical conductivity enabled electrical signal transmission between the spacecraft and the antenna dish (Rawal, 2001).

MMC are not limited to mechanical applications, there use in the biomedical industry has been explored as well. Magnesium metals can be used in orthopedic surgeries as temporary implants such as wire, rods, pins, plates, screws, etc. This is because of its biocompatibility and biodegradable property which makes secondary surgery to remove implants obsolete. Mg composites have been explored to control the corrosion rate, ensuring temporary implants do not degrade before the tissue is healed (Bommala et al., 2019).

Ceramic reinforcements such as TiC, Ni and ZrO_2 have been added to various industrial operations including cutting, rolling, stamping, piercing, drawing, and punching to improve the strength, toughness and hardness of the material performing the operation (Saxenaa et al., 2017). Ceramic MMCs have also been explored as potential tooling materials for friction stir welding of various metals with large differences in welding temperatures. TiC based ceramic metal composites and WC-Co were tested and compared, outperforming stainless steel in terms of wear resistance (Kolnes et al., 2020).

3. Experimental Methodology

This chapter describes the experimental methods used in this thesis focusing on the processing and characterization of the metal matrix composites. Details of the metal scaffold, and the development of the colloids are explained. The silicate colloid was chosen for its ease of use and low temperature curing process, which are potentially favorable when developing a composite with an existing scaffold. Zirconia was chosen for developing a MMC with significantly improved material properties. Details of the individual infiltration methods, sintering methods, and resulting porosities are explained.

3.1. Materials

3.1.1. Hastelloy-X Scaffold

The Hastelloy-X scaffolds that are the matrix of the MMCs were provided by the Technetics Group Deland, FL facility. The manufacturing process first consists of felting raw fiber into sheets. The Hastelloy-X fibers are cleaned and sifted to remove aggregates then dispersed to create fiber sheets. The sheets are then vacuum sintered to form diffusion bonds between fibers. These sintered sheets are formed to a final porosity of ~80%.

Figure 3.1 Hastelloy-X Scaffold.

3.1.2. Zirconia

Zirconium (IV) oxide-yttria stabilized (linear formula ZrO_2, Y_2O_3) submicron powder was ordered from Sigma-Aldrich headquartered in St. Louis, MO. The powder contains ~8 wt.% yttria as the stabilizer, particle size of ~700 nm and is 99.9% purity trace metals basis (purity excludes ~2%HfO_2) (“Product Specification Zirconia(IV)”, n.d.).

3.1.3. SDS

Dispersants are beneficial to particle dispersion by breaking apart agglomerates. Studies have shown that without dispersants, particles sizes can increase drastically affecting composite manufacturing (Amat et al., 2013). Sodium n-dodecyl sulfate (SDS) ($CH_3(CH_2)_{11}OSO_3Na$), 99% (dry wt.), water <1.5% supplied by Alfa Aesar (headquartered in Haverhill, MA) was used as a dispersant for the zirconia colloid. In a study it was found that a similar dispersion agent, sodium dodecylbenzene sulfonate (SDBS), did aid in particle dispersion for a zirconia nanofluid. Resulting in less agglomeration compared to nanofluids that were processed without SDBS (Ordoneza et al., 2020).

3.1.4. Dichtol

The silicate colloid used is trade named Dichtol HTWG Hydro #2506 and was purchased from Diamant Coating Systems Stronghold Coating in Sharonville, OH. Its chemical composition is proprietary, but the basic component is silicate. Infiltration is rated for pore sizes less than 100 µm (“Dichtol HTWG Hydro Product number”, 2018).

3.2. Colloid Preparation

3.2.1. Zirconia

The zirconia colloid was created with varying weight percentages of zirconia, SDS as a dispersant and distilled water as the dispersion media. The colloids were first magnetically stirred using a Troemner (model number 984T47CHSUSA) advanced top hotplate stirrer for 45 min, then continuously ultrasonicated, using a Sonics VCX-600 watt ultrasonic processor with probe, for 15 minutes at 21°C at a amplitude of 40% (Rami et al., 2009; Amat et al., 2013; Vasylkiv & Sakka., 2001).

Table 3.1

Zirconia Colloids Weight Percent

Chemical	**Colloid 1**	**Colloid 2**	**Colloid 3**
Zirconia (wt%)	15	25	50
SDS (wt%)	5	5	5
Distilled Water (wt%)	80	70	45

3.2.2. Dichtol

Dichtol is “a ready to use, water-based one component system for impregnation of materials” (“Dichtol HTWG Hydro Product number”, 2018, p. 1) Dichtol is unique in the fact that neither vacuum nor pressure is required. Infiltration is achieved by its capillary activate impregnation and can be applied via brushing, spraying, injecting, or dipping (“Capillary-active impregnation”, n.d.).

3.3. Colloid Preparation

3.3.1. Wet Layup

A aluminum plate was sanded and cleaned with acetone. After drying a thin layer of a release agent, 1153 FibRelease produced by FibreGlast in Brookville, OH, was brushed over the plate and allowed to dry for 5 minutes. Scaffolds were then placed on the aluminum plate and the colloid was poured over and rolled into the samples. This process repeated until the colloid could be seen pooling on the aluminum plate. The samples were covered with a peel ply sheet and then a breather sheet. The air seal was constructed using a vacuum bag fixed to the edges of the aluminum plate using double sided sealant tape. A vacuum plate and a Dentsply MaxVac pump (part number 9494198) were used to generate the vacuum.

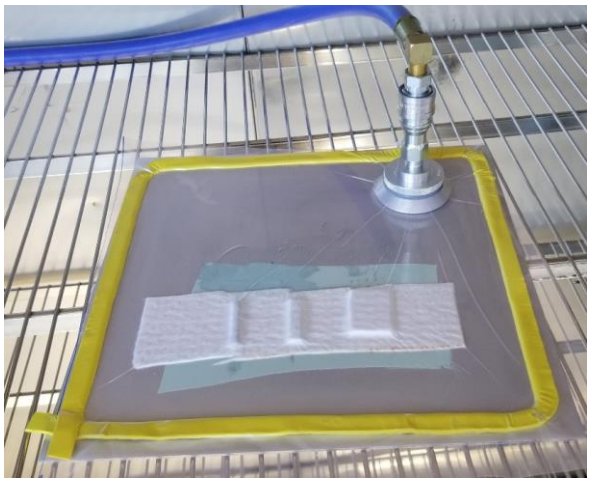

Figure 3.2 Wet Layer Setup.

3.3.2. Vacuum - Air Cure

Samples were placed in individual containers, the colloid was then poured in the containers until the samples were completely submerged. The containers were then

placed in a Ted Pella Inc. desiccator (product number 2246-1) or a ProCraft bell jar (model number 17016) depending on availability of devices. A vacuum was then applied until air bubbles could no longer be seen escaping from the samples, ~5 min. The vacuum was then released, samples were removed from the bell jar or desiccator, then removed from the colloid and air cured for 48 hr.

Figure 3.3 Desiccator Setup.

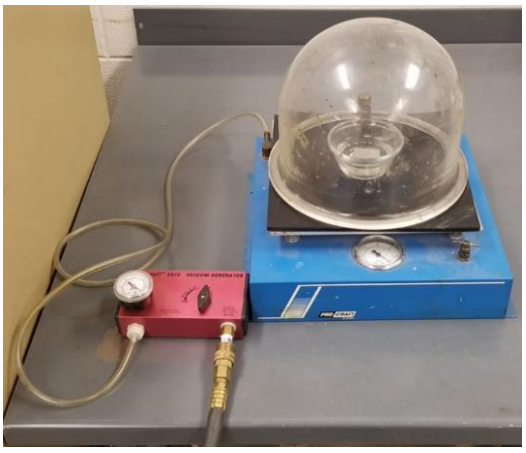

Figure 3.4 Bell Jar Setup.

3.3.3. Submerge Cure

Scaffolds were placed in individual glass containers, then the colloid was poured in the containers until the samples were completely submerged. For 48 hr the samples were allowed to cure while submerged. Afterwards the samples were removed from the container and allowed to air cure for 24 hr. Submerged curing that extended beyond 48 hr resulted in the samples breaking upon removal from the cured colloid pool. The force required to separate the composite from the cured colloid which bonded to the glass container surfaces exceeded the composites strength which resulted in some composites breaking during removal. The submerge cure method resulted in a excess amount of the silicate colloid partially curing on the surfaces of the samples after submersion. This excess was immediately removed before air curing, any excess colloid allowed to air cure became difficult to remove without damaging the sample. This excess was removed to prevent influencing the porosity calculations. The purpose of the method is for the colloid to infiltrate and cure within the sample.

3.3.4. Vacuum – Submerge

The samples were placed in individual glass containers, the colloid was then poured in the containers until the samples were completely submerged. The containers were then placed in a desiccator or bell jar and a vacuum was applied for 24 hr or 48 hr depending on which timeframe was tested. The vacuum was then released, samples were removed from the desiccator or bell jar and air cured for 48 hr while submerged. Afterwards the samples were removed from the container and allowed to air cure for 24 hr. As seen in the submerge cure method, a excess amount of the silicate colloid was seen partially cured on the top surface. This excess was removed before the samples were allowed to air

cure.

3.3.5. Vacuum - Pull Through

A compressed air line was connected to a TMI Hold Fast Vacuum Generator (part number V812). This device works by forcing air through a conical Venturi orifice. As the compressed air makes its way from the restricted conical orifice to the larger open lines the pressure decreases and the velocity increases. This creates a vacuum and the air meant to be evacuated from the system is pulled into the flowing airstream and blown out (Ormer, 2013). The vacuum line from the Vacuum Generator was connected to a filtering flask fitted with a Bel-Art polypropylene 315 ml two piece Buchner funnel.

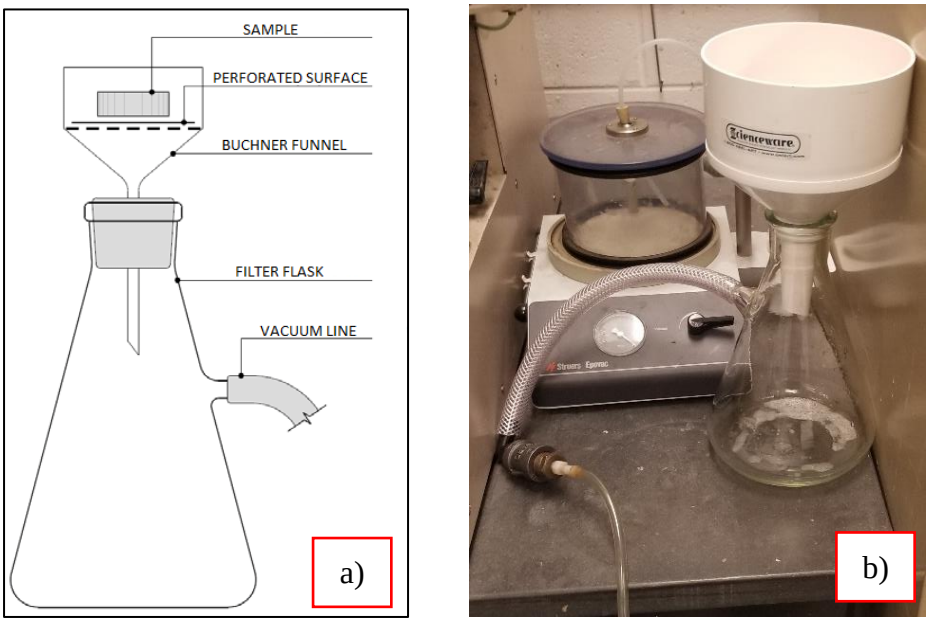

Figure 3.5 Vacuum - Pull Through Setup a) Example b) Actual.

Silicone gasketing material and Tartan box sealing tape (product number 302) were used to seal the sample to the perforated funnel to ensure the vacuum was drawing air

through the sample and not around it. By placing a plastic sheet over the sample, a vacuum of less than -15 kPa was verified on the gauge before all tests were performed.

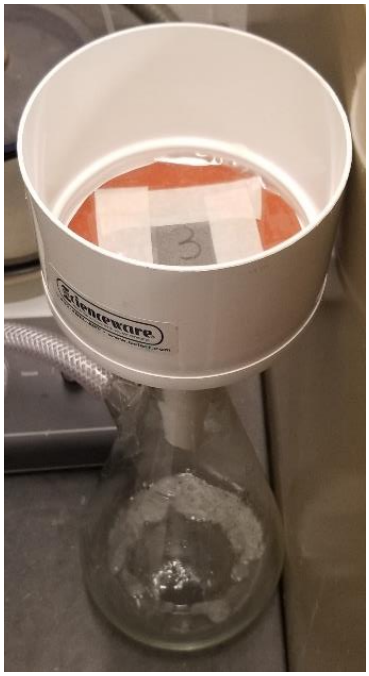

Figure 3.6 Vacuum - Pull Through Sample Setup.

The colloid was poured on the top surface of the sample with the vacuum applied until sufficient colloid could be seen at the bottom of the flask, indicating full penetration through the sample. The vacuum was shut off while the colloid was being poured with the intent of trapping as much of the colloid within the sample as possible. After 24 hr of curing, the process was repeated, this cycle continued until minimal change in porosity was measured after curing. The measurement method will be explained later in this thesis. This method was developed in response to the noticeable amount of the colloid curing on the surface of the samples that were infiltrated using the submerge methods.

The concern was whether the colloid was successfully infiltrating the interior of the samples or concentrated mainly on the top surface. High concentrations of the cured silicate colloid were not seen accumulated on the surface of the vacuum pull through samples.

3.4. Sintering

3.4.1. Zirconia

Colloid composition, processing, and sintering program were in accordance with similar research using zirconia MCCs (Tarabay et al., 2012; Molin, et al., 2011; Dourandish, et al., 2008). Samples were sintered according to the following program, see Fig 3.7:

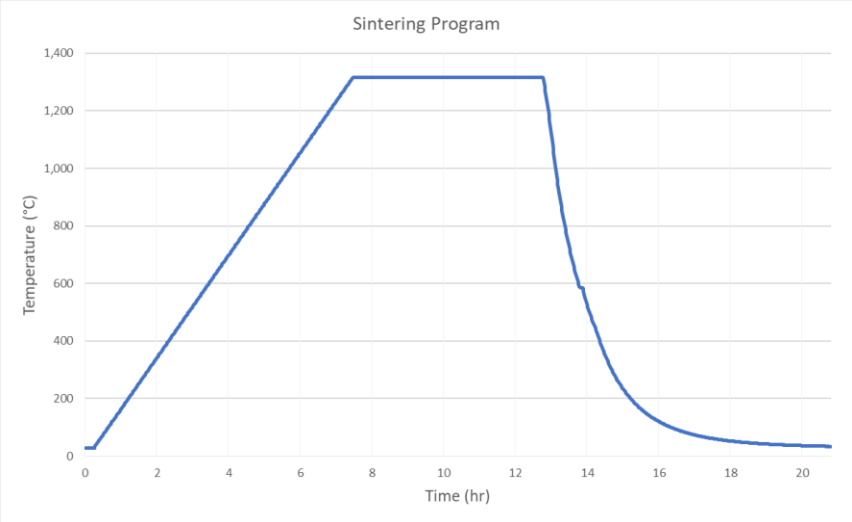

Figure 3.7 Sintering Program

1. Ramp up to 1350°C in partial pressure H_2
2. Dwell at 1350°C for 4 hr in partial pressure H_2

3. Ramp Down to 482°C
4. Force cool to 37°C using nitrogen

The samples were sintered in a vacuum furnace from Vacuum Furnace Systems Corp. with a maximum operating temperature of 1,482°C, maximum internal operating pressure of 0.103 MPa and gas cooling up to 56 m^3/min using a Eurotherm 2404 controller.

Figure 3.8 Vacuum Furnace Systems Corp. Vacuum Furnace.

3.4.2. Dichtol

The silicate colloid does not require any heat treatment for curing. It partially cures in 24 hr and fully cures in 48 hr at room temperature.

3.5. Porosity Measurements

There are several methods that can be used to measure porosity. The most common ones are described below as well as which method was used for porosity measurements in this thesis.

3.5.1. Archimedes Method

The dry mass of the scaffold is measured (M_{dry}), the scaffold is then prewet with ethanol and submerged in water under negative pressure, the submerged mass is recorded ($M_{submerged}$). The scaffold is then removed from the water and its wet mass is recorded again (M_{wet}). This method would not be used for hydrophobic polymers scaffolds, it's difficult for water to penetrate the pores and water causes shrinkage or swelling in polymeric scaffolds (Hoa & Hutmachera, 2005).

$$Porosity = \frac{(M_{wet} - M_{dry})}{(M_{wet} - M_{submerged})} \quad (3.1)$$

M_{dry} = mass of the scaffold when dry

M_{wet} = mass of the scaffold when submerged in water

$M_{submerged}$ = mass of the scaffold once it's removed from water

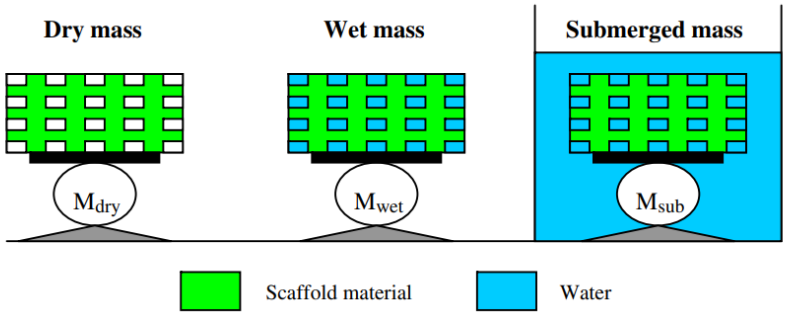

Figure 3.9 Archimedes Method (Hoa & Hutmachera, 2005, p. 1366).

3.5.2. Liquid Displacement Method

A known volume of ethanol is recorded (V_1), the scaffold is placed in ethanol under vacuum to remove any trapped air. The volume of the ethanol and the submerged scaffold are measured (V_2). The scaffold is then removed from the ethanol and the remaining volume of ethanol is measured (V_3). By using ethanol, the shrinkage and swelling issues associated with hydrophobic polymers scaffolds are avoided (Hoa & Hutmachera, 2005).

$$Porosity = \frac{(V_1 - V_3)}{(V_2 - V_3)} \tag{3.2}$$

V_1 = volume of ethanol

V_2 = volume of ethanol and the submerged scaffold

V_3 = volume of ethanol once the scaffold is removed

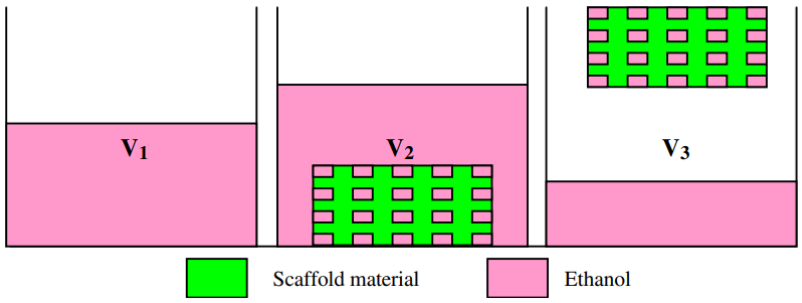

Figure 3.10 Liquid Displacement Method (Hoa & Hutmachera, 2005, p. 1367).

3.5.3. Mass Technique

For this thesis the initial porosity was measured using the same process used by Technetics Group in Deland, FL and seen in research. The process is referred to as the

mass technique which is sufficient for measuring the porosity of samples with simple geometries.

$$Porosity = \left(1 - \frac{V_g}{V_a}\right) * 100\% \quad (3.3)$$

V_g = volume of scaffold material

V_a = apparent scaffold volume

V_g calculates the volume of the sample by dividing the mass of the sample by the material density. V_a calculates the volume assuming the sample is solid (0% porosity) by multiplying the length, width, and height of the sample. The resulting porosity is only as accurate as the linear measurements required for the calculations. Irregular shapes, rough edges and non-perpendicular cuts can result in inaccurate measurements that affect porosity values (Ho, Hutmacher, 2005). The samples used for testing were rectangular in shape, with lengths and widths less than 38 mm and ~3.175 mm thick. Sample dimensions were measured using a Mitutoyo digital caliber (model number 500-196-30). Given this simple geometry the mass technique was deemed acceptable for porosity calculations. Porosity after infiltration was measured using the same process except V_g was calculated to account for the difference in density between the Hastelloy-X and the infiltrated chemical (silicate or zirconia). Weights were measured using a A&D analytical balance (HR-60 model).

$$V_g = \left(\frac{m_{initial}}{\rho_{Hastelloy-X}}\right) + \left(\frac{\left(m_{infiltrated} - m_{initial}\right)}{\rho_{zirconia}}\right) \quad (3.4)$$

3.6. Microstructure Characterization

Figure 3.11 FEI Quanta 650 SEM.

SEM imaging was conducted using a FEI Quanta 650 scanning electron microscope (SEM). Samples were prepared for imaging using a Struers polishing machine (abramin model) to wet polishing samples with waterproof silicon carbide paper up to 4,000 grit.

3.7. X-Ray Characterization

X-ray tomography was conducted using a Bruker Skyscan 1275 3D X-Ray Microtomograph.

Figure 3.12 Bruker Desk-Top X-ray Tomograph.

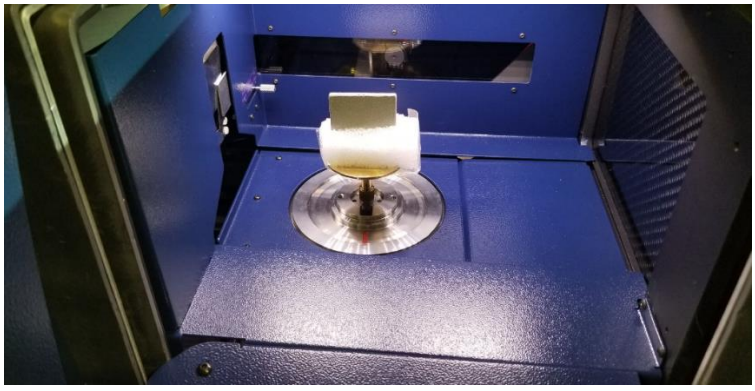

Figure 3.13 X-Ray Tomograph Sample Setup.

3.8. Hardness Testing

Hardness testing was performed using a ACCO Wilson Rockwell Hardness Tester. Testing was conducted according to ASTM Standard E18-15. It was determined that the HRL scale which utilizes a ¼ in ball indenter, 10 kg minor load, and 60 kg major load provided the appropriate range for the samples.

Figure 3.14 ACCO Wilson Rockwell Hardness Tester.

3.9. Nanoindentation

Nanoindentation was performed within a MBRAUN laboratory glovebox (model number MB-200B) using a Bruker nanoindenter. Samples were polished using the same method for SEM preparation and fixed to steel plates using Hardman double/bubble epoxy extra fast setting.

Figure 3.15 Bruker Nanoindenter.

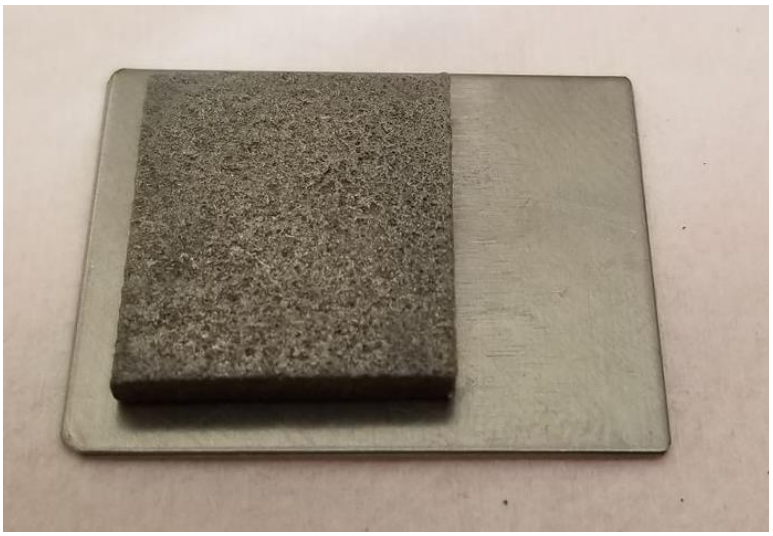

Figure 3.16 Nanoindentation Sample Setup.

4. Results and Discussion

After fabrication of the composites, porosity was calculated and compared between the various infiltration methods. SEM and x-ray tomography was conducted to further investigate infiltration effectiveness and identify any anomalies in the microstructures. Material properties were evaluated by measuring, Rockwell hardness and through nanoindentation. Nano-scratch testing was attempted to further evaluate material properties. Due to the porous nature of the scaffold, even after polishing, the surfaces of the samples were too rough for definitive results. The results for these various aspects are described below followed by a discussion.

4.1. Porosity Measurements

4.1.1. Porosity of Zirconia-Hastelloy-X Composite

The vacuum submerge method was used to infiltrate the scaffold with the zirconia colloid. As the zirconia weight approached 50%, the colloid viscosity increased. 50 weight percent was deemed sufficient to create a noticeable change between the scaffold and the newly created composite's material performance. Therefore, colloids with greater than 50 weight percent zirconia were not pursued. As expected, the colloid with the highest weight percent of zirconia had the lowest porosity, average of 59%. A comparison of the other zirconia weight precents and resulting porosities can be seen in Figure 4.1.

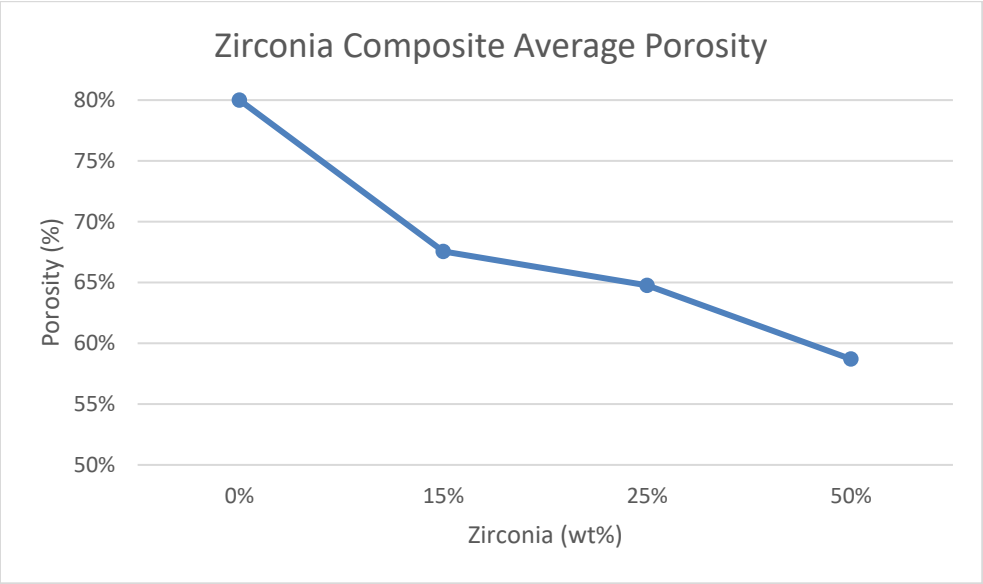

Figure 4.1 Porosity in the Zirconia-Hastelloy-X Composites.

4.1.2. Porosity of Silicate-Hastelloy-X Composite

The average porosity after infiltration using the methods described for the silicate colloid were measured and compared to the initial 80% porous scaffold. The wet layup and vacuum-air cure methods had the least effect on the porosity and the greatest range, with average porosity reductions of 12% and 13% respectively. The colloid could be seen infiltrating the sample, but without a partial cure, the viscosity of the colloid allowed it to pass through the sample without curing in the interior. It was determined that the wet layer and vacuum-air cure infiltration methods were inefficient.

Porosity was most consistent during the submerge cure method with a average of 54% and a standard deviation of 0.283. When vacuum was used in addition to submersion the resulting average porosity only decreased by 2% while the standard deviation increased up to 1.814. This was the case for the 12 hour and 24 hour vacuum

submerge cure method. In all three methods, it was evident that all of the colloid did not cure within the sample, a layer of the colloid cured on the surface of the samples. The minimal difference in porosity and consistent buildup of colloid on the surface when vacuum was applied indicates that the combination of submersion and vacuum does not significantly increase infiltration for the silicate colloid.

The vacuum pull through method gradually reduced the porosity of the samples to a average of 57%. While still higher than the submerge method average porosity, there was no noticeable amount of the colloid that cured on the surface.

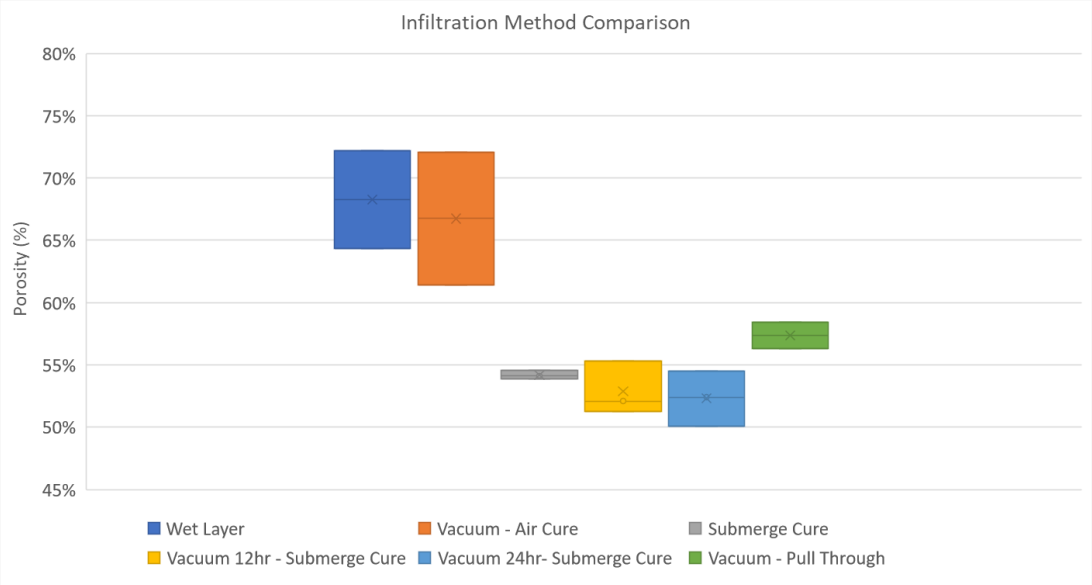

Figure 4.2 Infiltration Comparison Graph.

In the vacuum pull through method, a “pull” is defined as one cycle of vacuum infiltration and a 24 hr cure. From the graph (Figure 4.23), five “pulls” were required before the curve began to level.

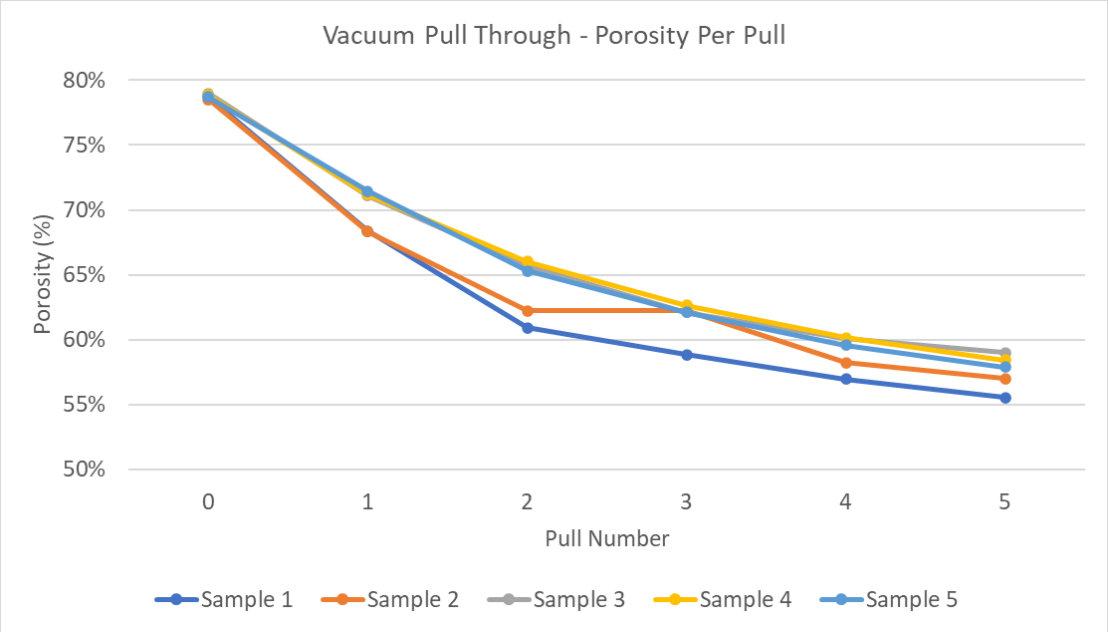

Figure 4.3 Vacuum Pull Through – Porosity Per Pull.

4.2. SEM

4.2.1. SEM Analysis of Non-Infiltrated Scaffold

The non-infiltrated scaffold provided by Technetics Group in Deland, FL are manufactured to have a porosity of 80%. As the fibers are sintered, they fuse together, randomly creating the porous structure which can be seen throughout the scaffold. The length and arrangement of the pores varies as can be seen in Figure 4.4 and Figure 4.5. This creates the tortuous path needed to minimize particle intrusion.

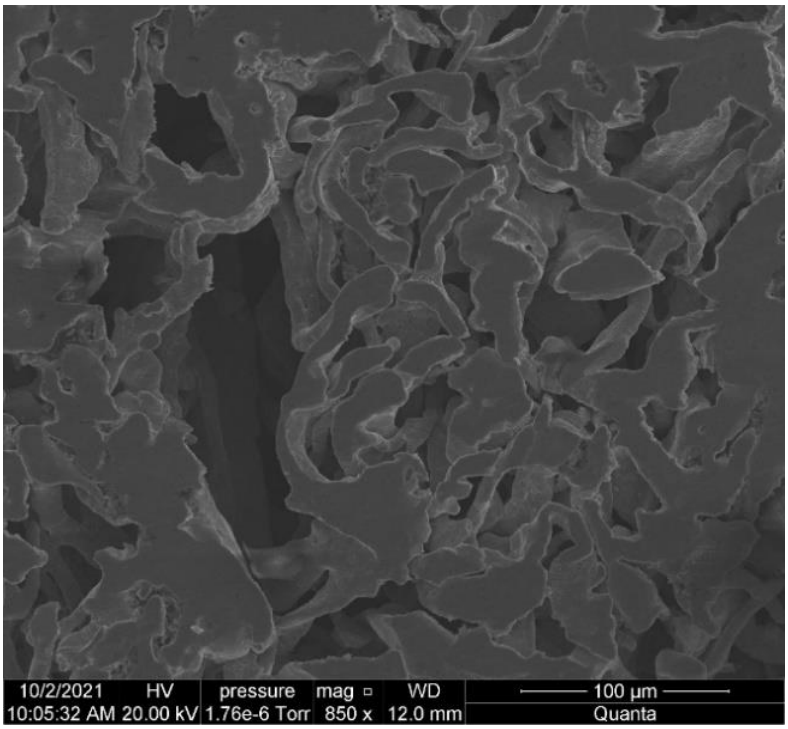

Figure 4.4 Non-Infiltrated – Cross Section a) 850CAPX.

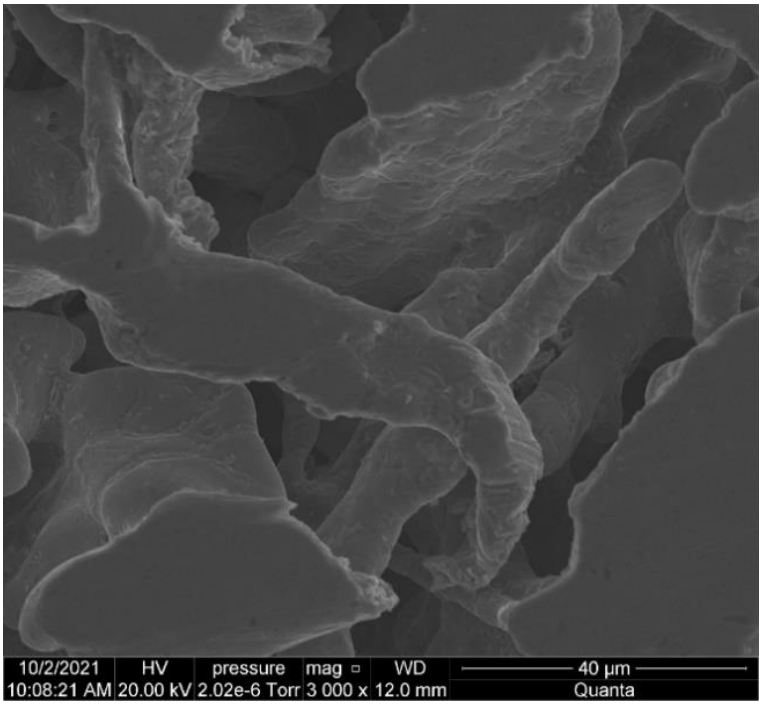

Figure 4.5 Non-Infiltrated – Cross Section 2,000CAPX.

There is no uniformity to the pore sizes, a random area of the non-infiltrated scaffold was measured. The resulting length of the pores ranged from 30 μm to 94 μm in Figure 4.6 but larger and smaller lengths were seen in other areas of the same sample. Individual fiber size was also measured, Figure 4.7, with resulting widths between 10 μm to 28 μm. Larger and smaller fiber widths were measured in different areas of the same sample. These lengths and widths depend largely on how effective the manufacturing process was in separating agglomerates and how the individual fibers contacted each other during sintering.

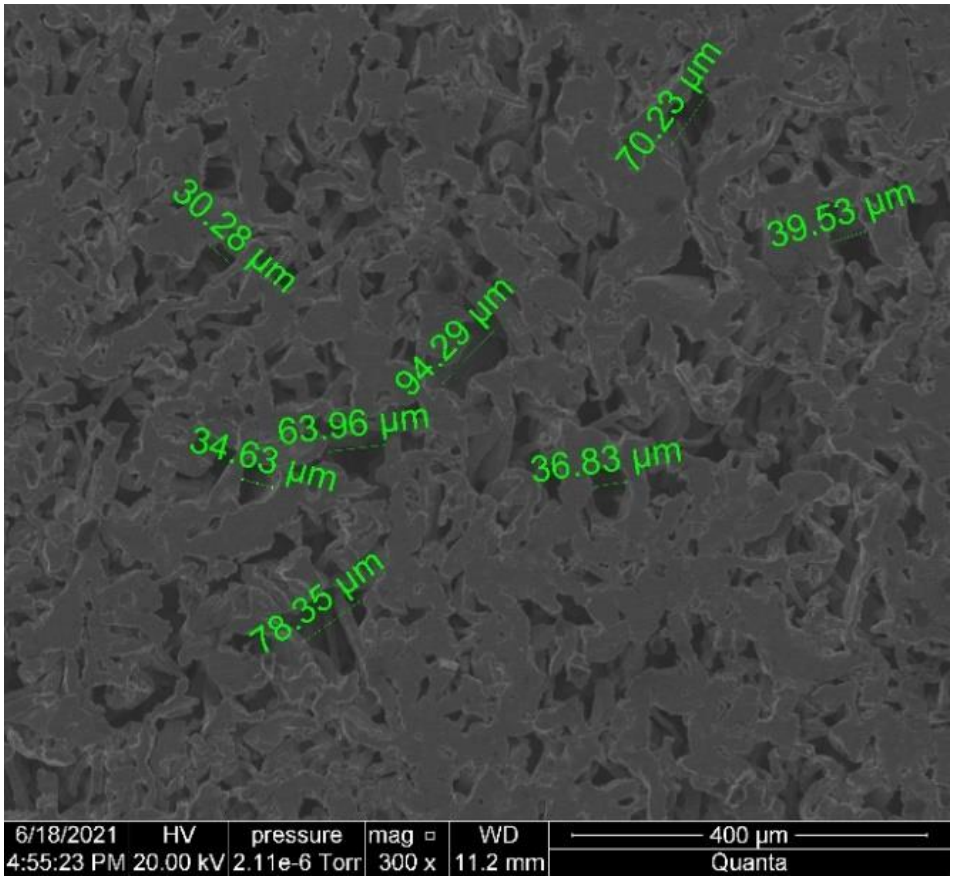

Figure 4.6 Non-Infiltrated – Cross Section 300CAPX.

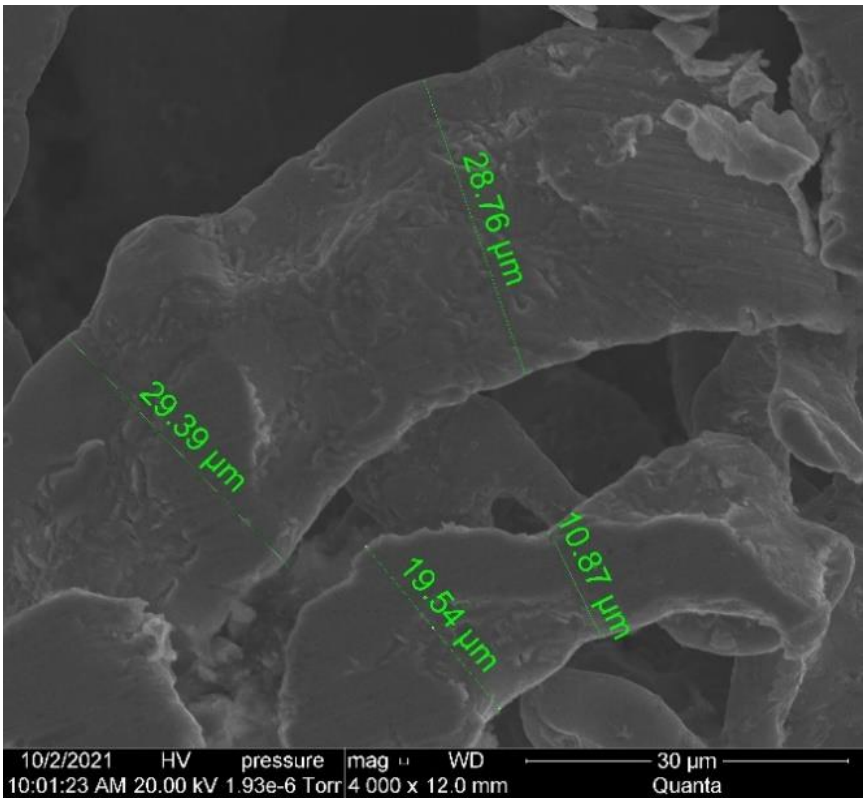

Figure 4.7 Non-Infiltrated – Cross Section 4,000CAPX.

4.2.2. SEM Analysis of Silicate – Submerged Composite

The submerge infiltration method resulted in a buildup of the cured colloid on the top surface where the colloid initially made contact. Even after attempting to remove the excess colloid from the surfaces of the sample after partial curing, the buildup can be seen in Figure 4.8. The top surface consists of a series of cracks that form cured colloid plates. The spacing between these plates measures up to ~13 µm, smaller cracks split off these plates, measuring ~4 µm in width, Figure 4.10. Within the sample, cross section images show crack lengths between the cured colloid of less than 2 µm, Figure 4.11.

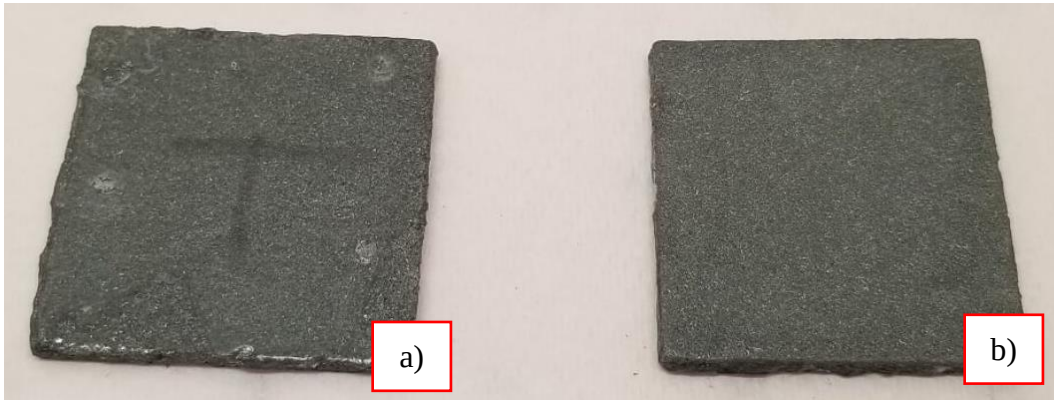

Figure 4.8 Silicate – Submerge a) Top Surface b) Bottom Surface.

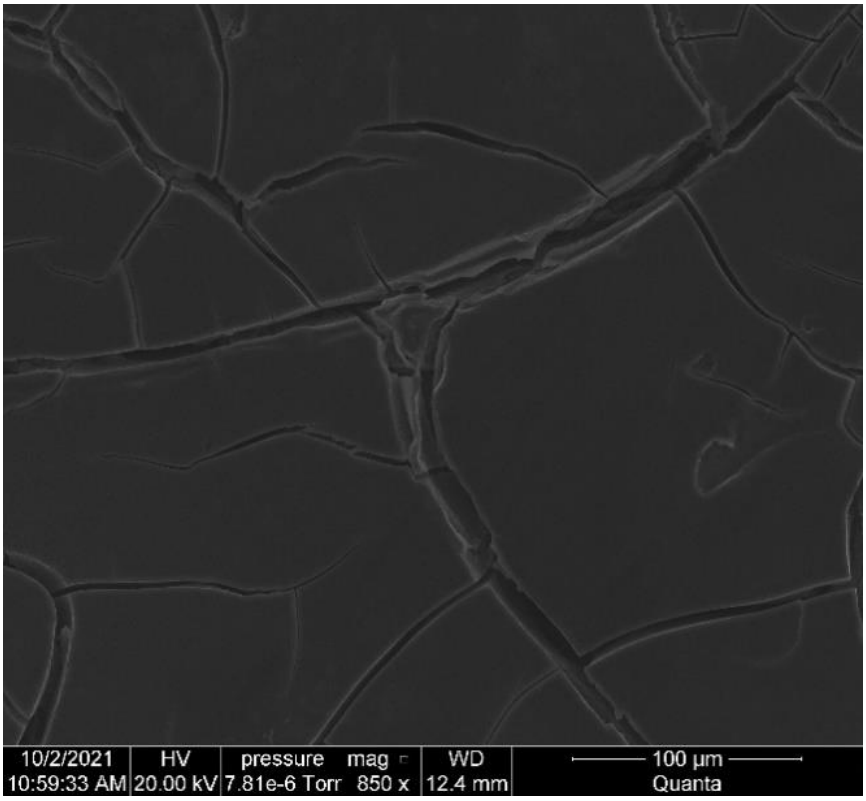

Figure 4.9 Submerge – Top Surface 850CAPX.

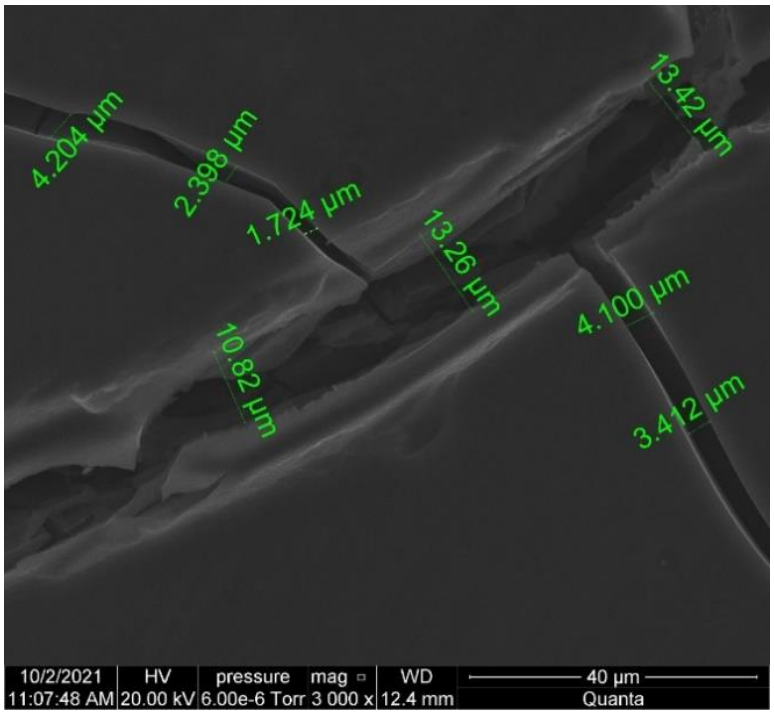

Figure 4.10 Submerge – Top Surface 3,000CAPX.

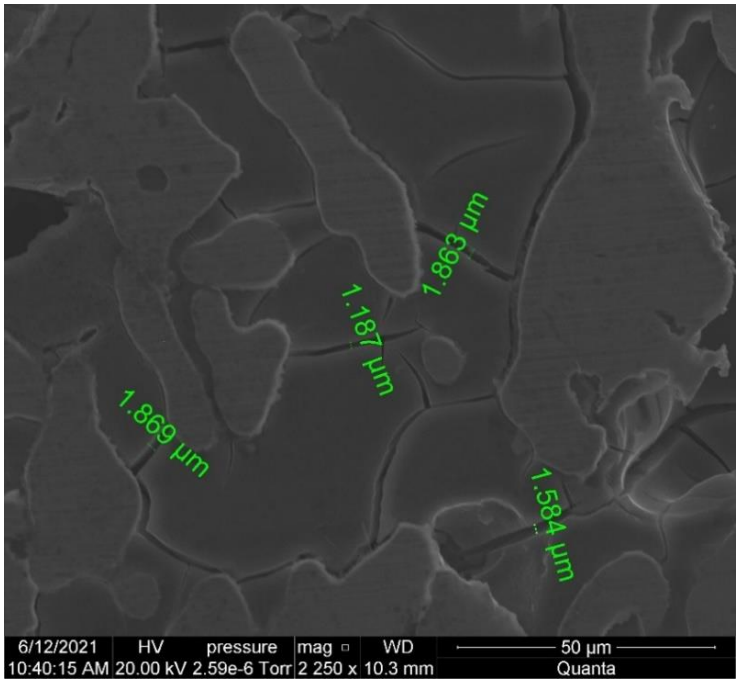

Figure 4.11 Submerge – Cross Section 2,500CAPX.

Cross section images confirmed that the buildup of silicate was limited to the top surface. From Figure 4.12, there is consistent infiltration along the right side of the image (top surface of composite), the uniform infiltration depth was measured in several areas. On average the uniform depth was between 450 μm and 550 μm with a few outliers, Figure 4.12. In contrast, Figure 4.13 shows a inconsistent infiltration along the left side (bottom surface of composite).

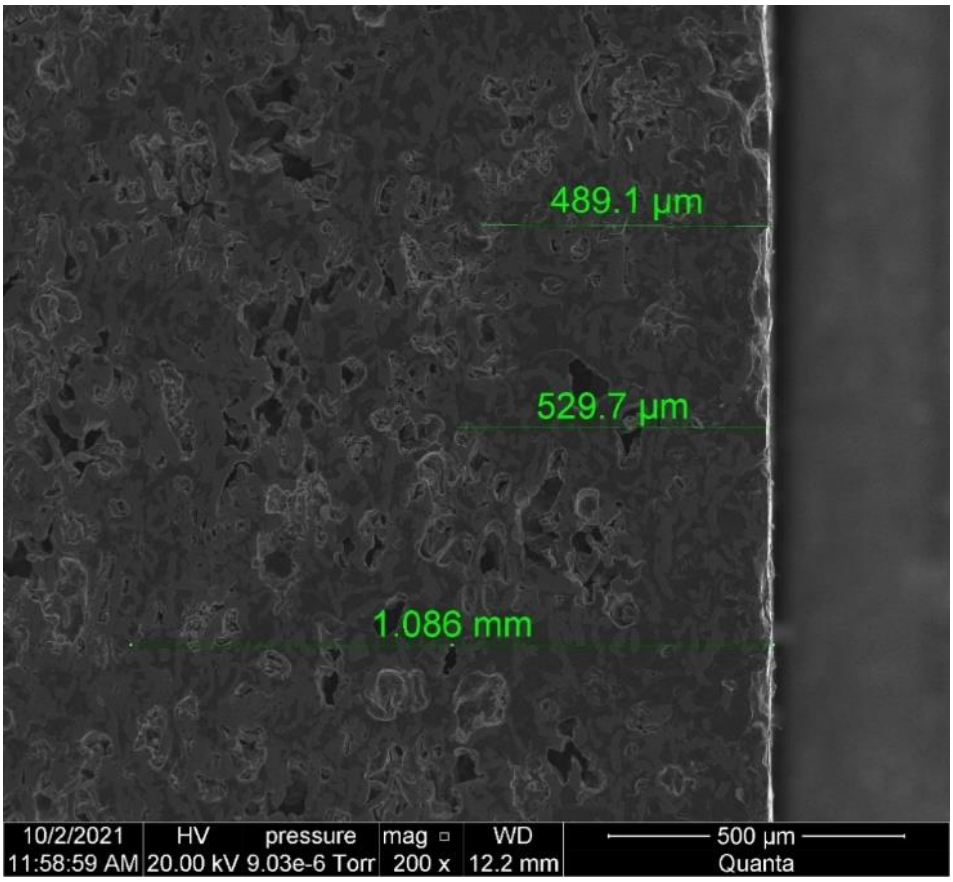

Figure 4.12 Submerge – Cross Section Top Surface.

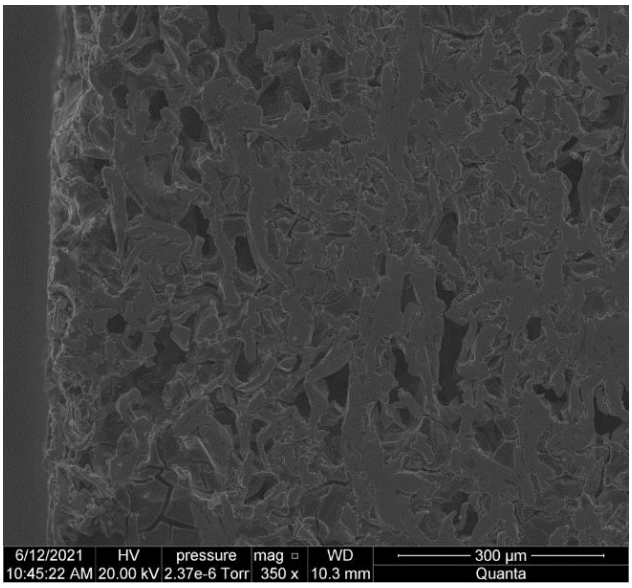

Figure 4.13 Submerge – Cross Section Bottom Surface.

In some areas, the colloid did perform as intended, carrying the silicate colloid into the pores, and curing around the Hastelloy-X fibers as seen in Figure 4.14 and Figure 4.15.

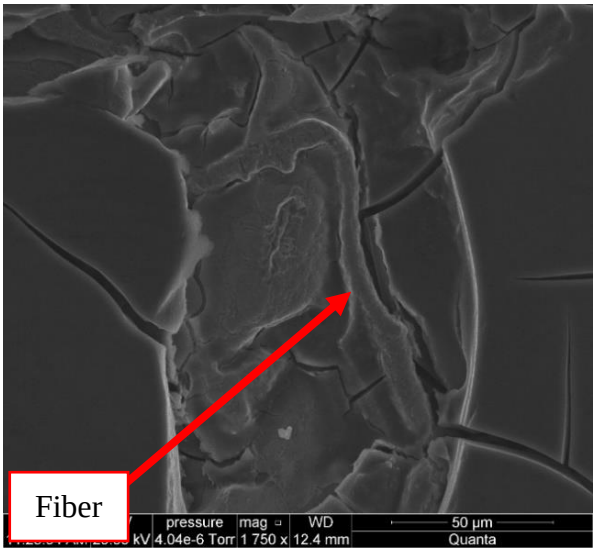

Figure 4.14 Submerge – Top Surface 1,750CAPX.

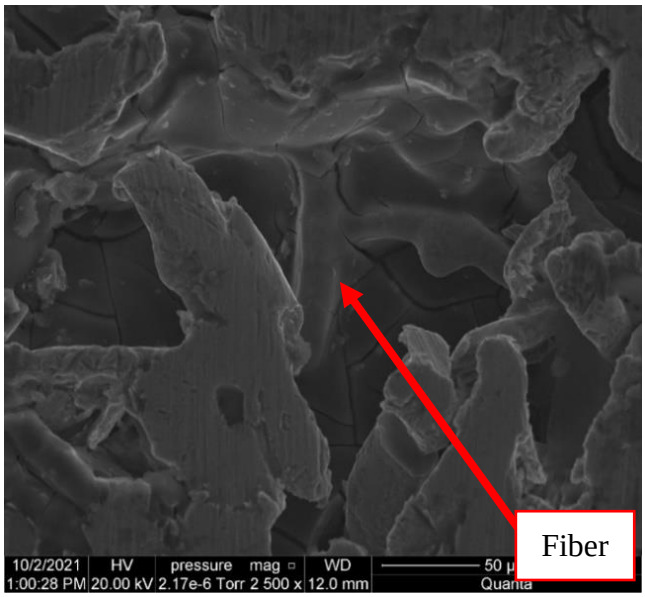

Figure 4.15 Submerge – Top Surface 2,500CAPX.

However, there was limited infiltration throughout the composite. In Figure 4.16, the cross section shows how the silicate colloid was able to infiltrate some pores of the composite but unable to access others.

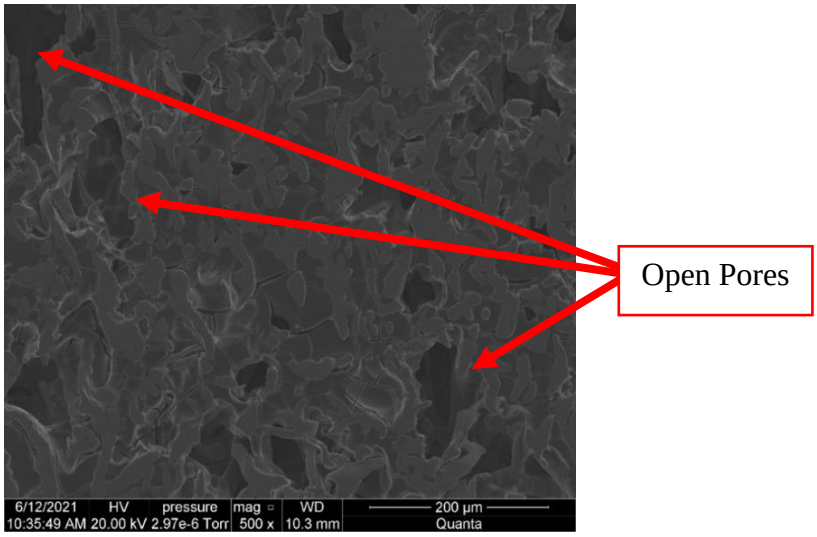

Figure 4.16 Submerge – Cross Section 500CAPX.

4.2.3. SEM Analysis of Silicate – Vacuum Pull Through Composite

The buildup of silicate on the top surface of the composites was not observed in the vacuum pull through composites. Imaging alone it not sufficient to determine if the vacuum pull through method is more successful than the submerged methods at infiltrating the interior of the scaffold. However, the resulting porosity from the method is comparable to the submerge method.

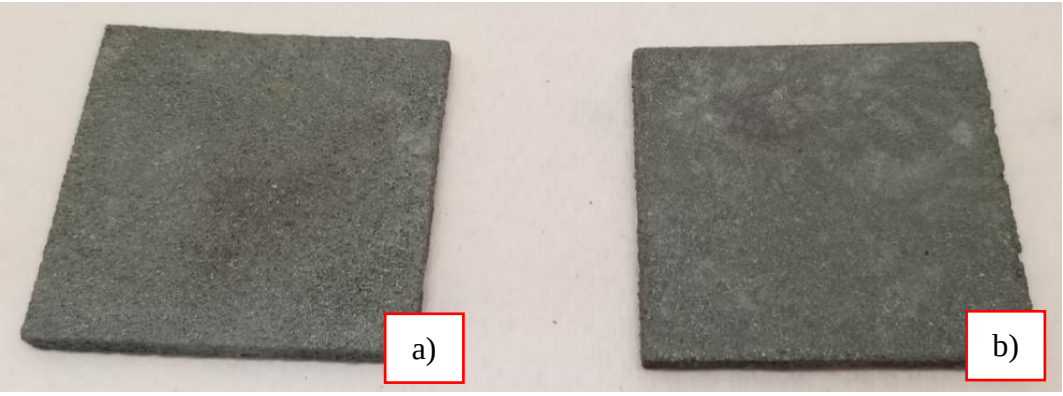

Figure 4.17 Silicate – Vacuum Pull Through a) Top b) Bottom Surface.

From the top surface images, Figure 4.18, the silicate colloid cured around the fibers as in the submerge method with some pores still left unfilled. However, the silicate particles were more prominent in the vacuum pull through method. Instead of remaining within the colloid, the particles are more exposed as evident in Figure 4.19. The prominence of the silicate was also seen in cross section images. With some areas having high concentrations of silicate particles compared to others, Figure 4.20. Silicate particles could be seen either attached to the Hastelloy-X fibers or in the cured colloid, Figure 4.21 and Figure 4.22, individual particle size ranged from 2 μm to 4.25 μm.

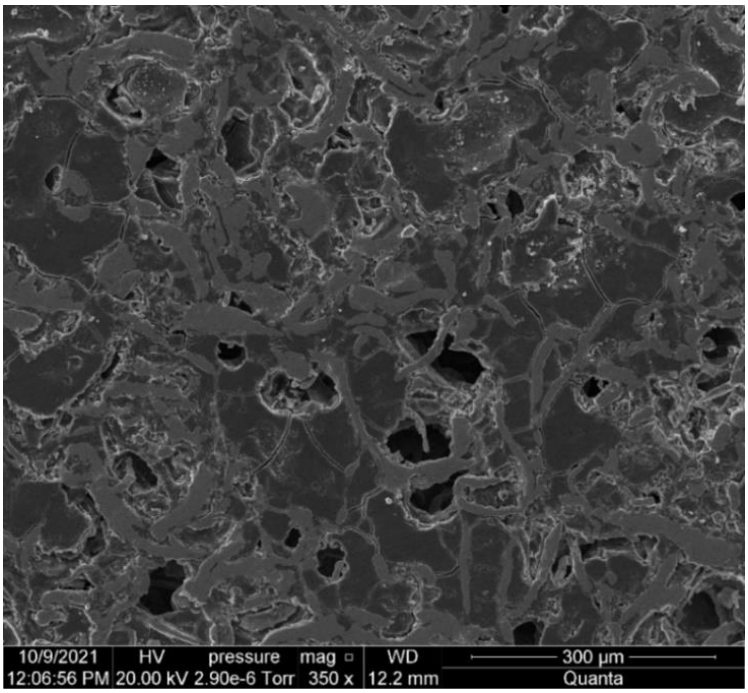

Figure 4.18 Vacuum Pull – Top Surface 350CAPX.

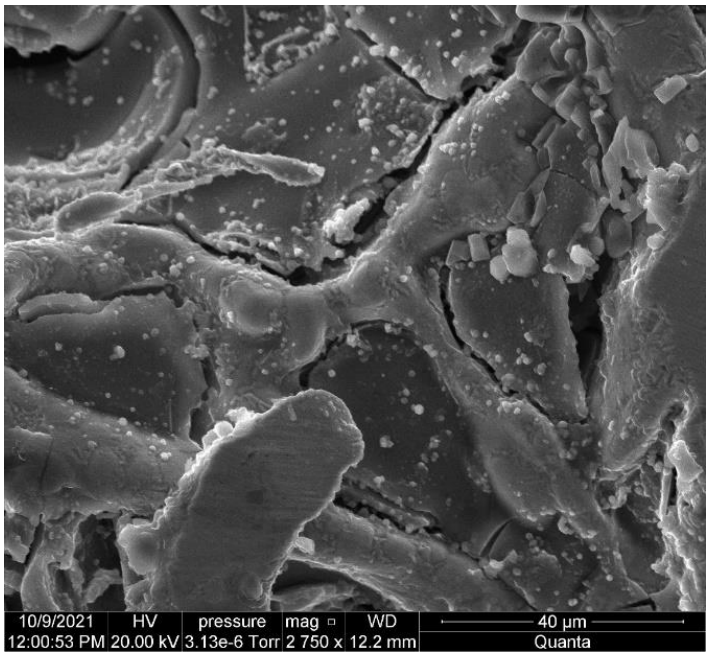

Figure 4.19 Vacuum Pull – Top Surface 2,750CAPX.

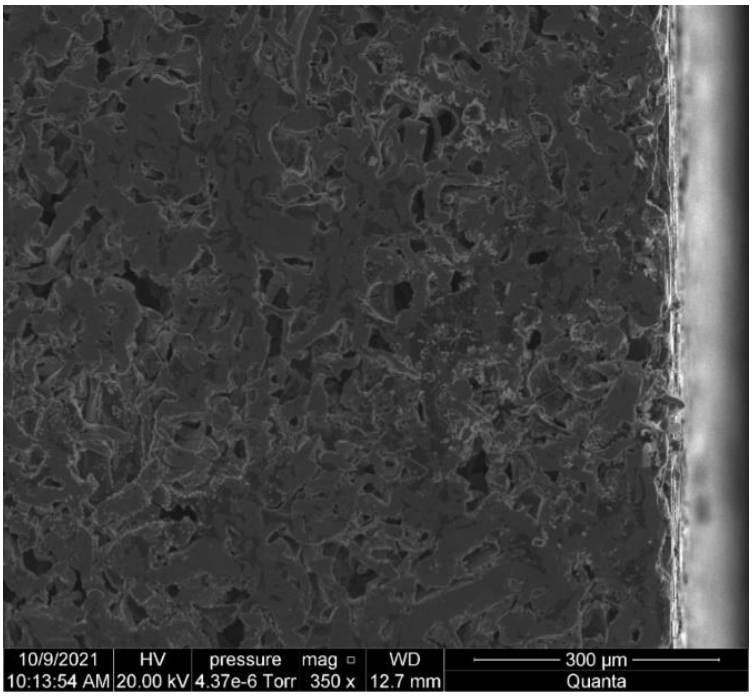

Figure 4.20 Vacuum Pull – Cross Section 350CAPX.

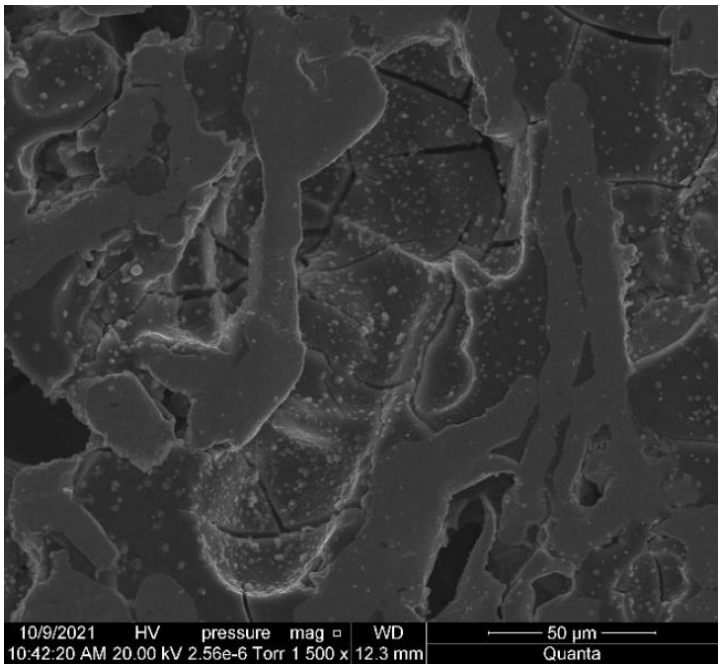

Figure 4.21 Vacuum Pull – Cross Section 1,500CAPX.

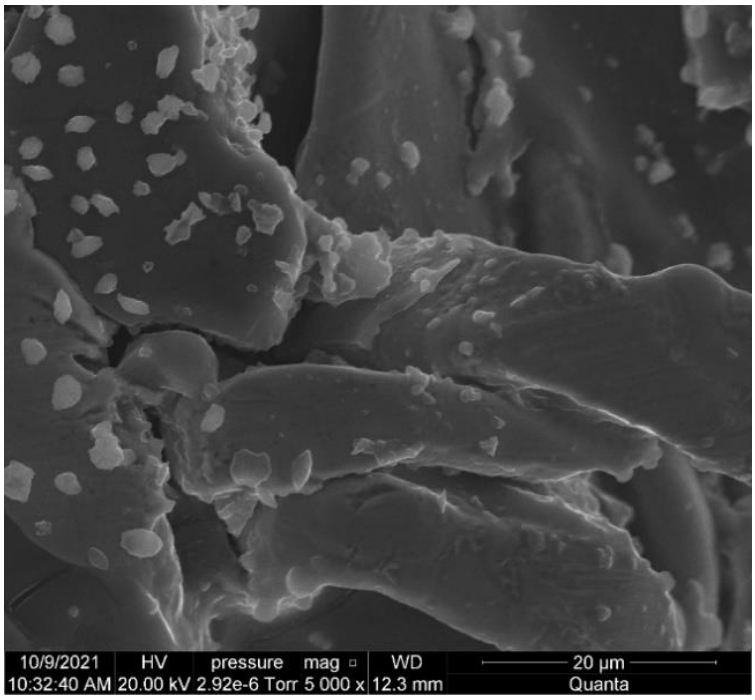

Figure 4.22 Vacuum Pull – Cross Section 5,000CAPX.

4.2.4. SEM Analysis of Zirconia – Vacuum Submerge Composite

After infiltration, the zirconia composites required sintering to cure unlike the room temperature curing silicate colloid. Top surface images from the same sample showed areas with relatively high concentrations of zirconia.

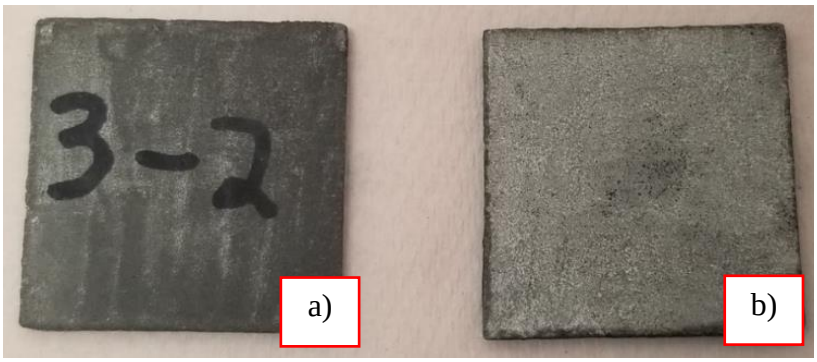

Figure 4.23 Zirconia – Vacuum Submerge a) Top b) Bottom Surface.

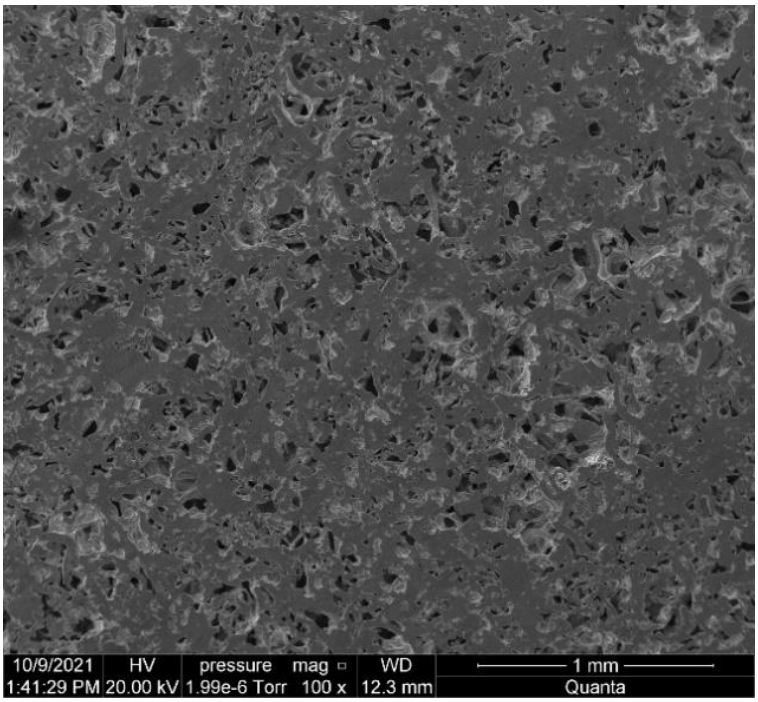

Figure 4.24 Zirconia – Top Surface Zirconia Concentration 100CAPX Low Concentration.

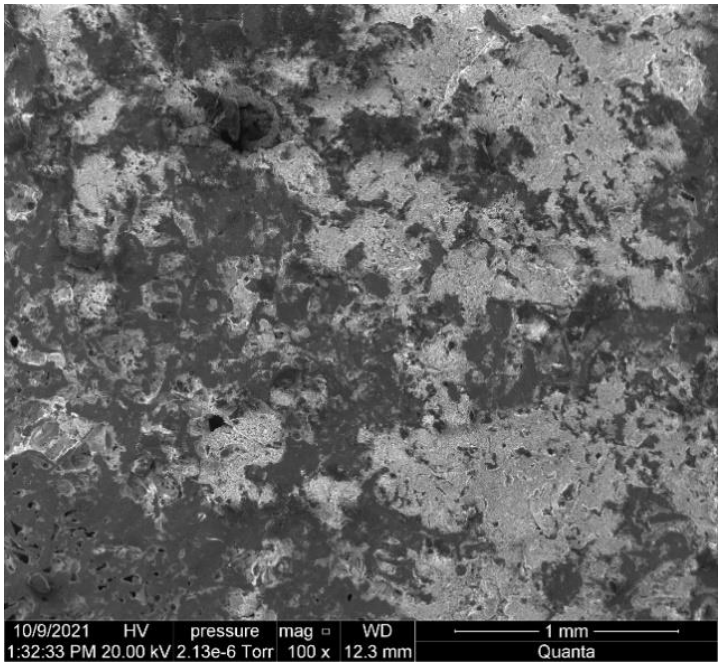

Figure 4.25 Zirconia – Top Surface Zirconia Concentration 100CAPX High Concentration.

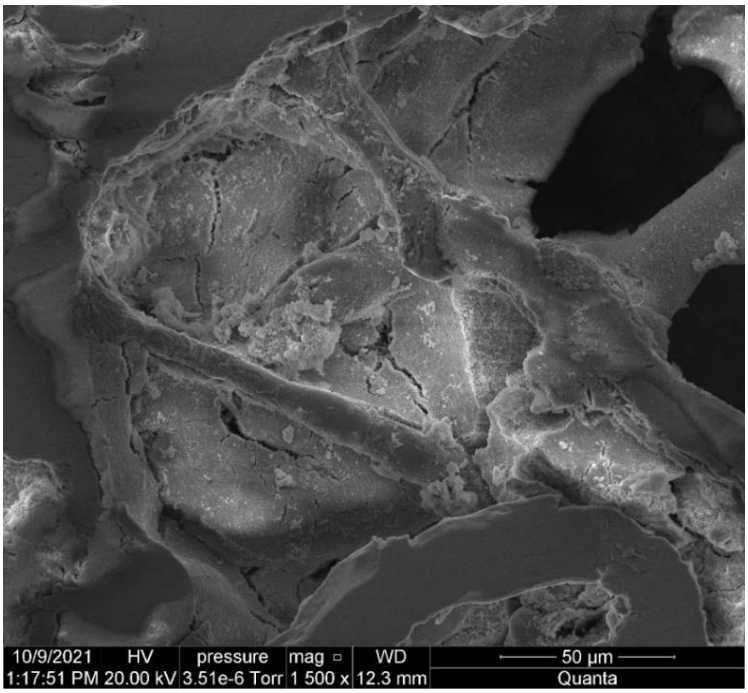

Figure 4.26 Zirconia – Top Surface 1,500CAPX.

Instead of filling the pores and curing around the Hastelloy-X fibers, the zirconia particles for the most part bonded to the fibers forming a thin layer, Figure 4.28. In some cases, agglomeration occurred where the zirconia particles bonded to other zirconia particles, Figure 4.29.

From imaging, a relatively consistent coat of zirconia is seen over various areas of the cross section. Infiltration was seen throughout the cross section of the samples, Figure 4.29 and Figure 4.30, indicated by the textured surface of the fibers vs the relatively smooth surface of the fibers from the non-infiltrated images. The largest particle sizes found were ~1.5 µm.

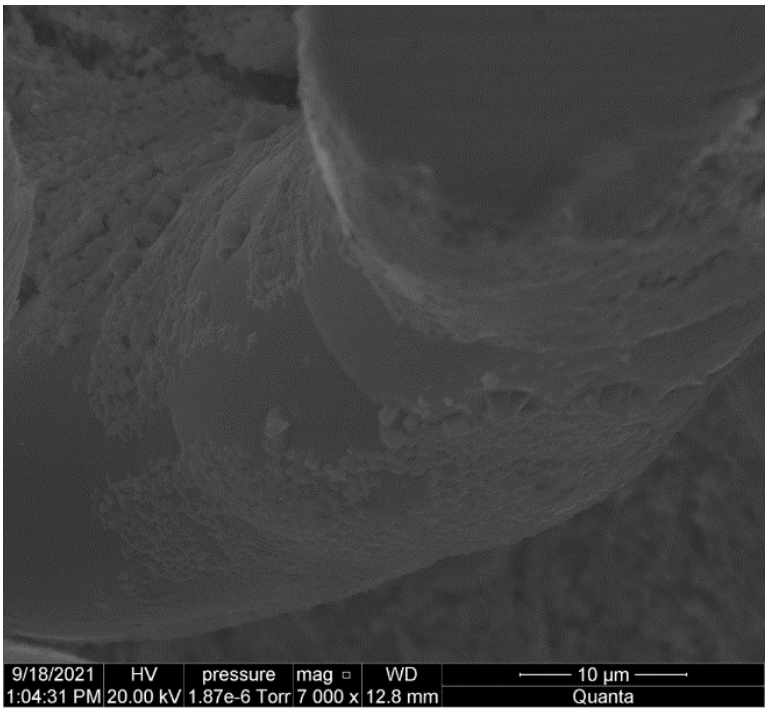

Figure 4.27 Zirconia – 7,000CAPX Cross Section.

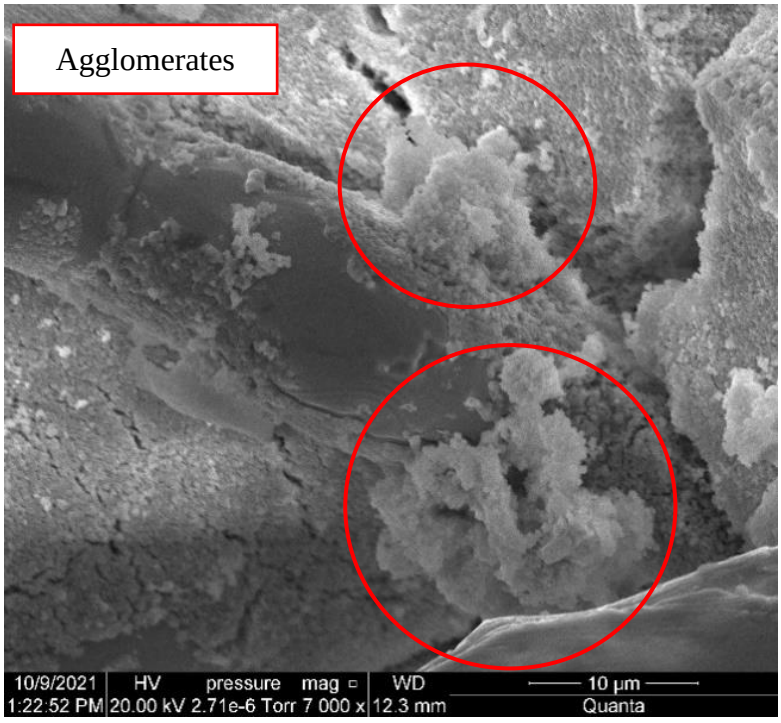

Figure 4.28 Zirconia – 7,000CAPX Top Surface.

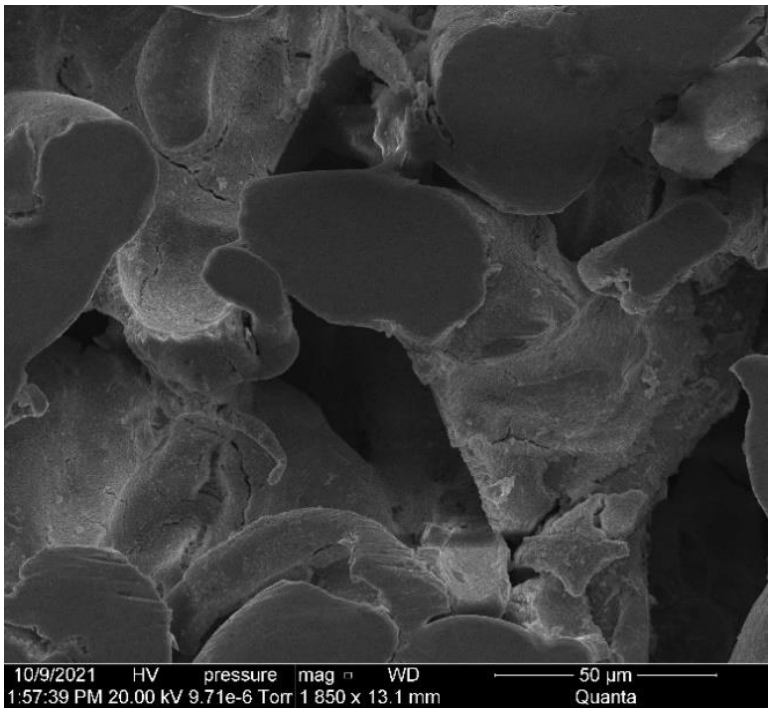

Figure 4.29 Zirconia – Cross Section 1,850CAPX.

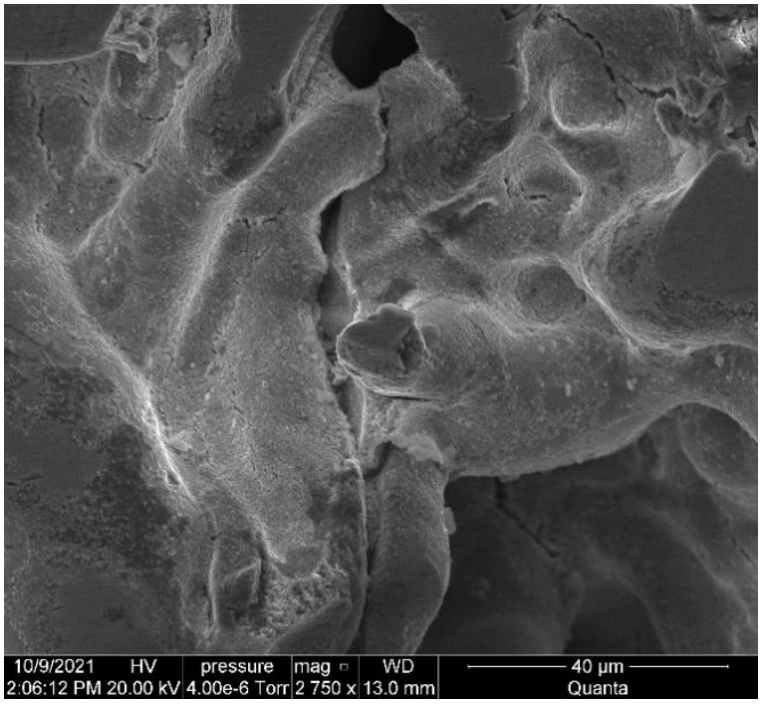

Figure 4.30 Zirconia – Cross Section 2,750CAPX.

4.3. X-Ray Tomography

Images of the non-infiltrated scaffold from multiple planes were taken. The Z-Y plane image remained consistent between the non-infiltrated, silicate – submerge and silicate – vacuum pull through. This makes sense given the pores that were infiltrated consisted of silicate particles dispersed within a cured colloid. Sufficient spacing between the particles would allow for better x-ray imaging. Darker areas were observed in the zirconia – vacuum pull through image, Figure 4.32, indicating areas the x-ray had difficulty penetrating.

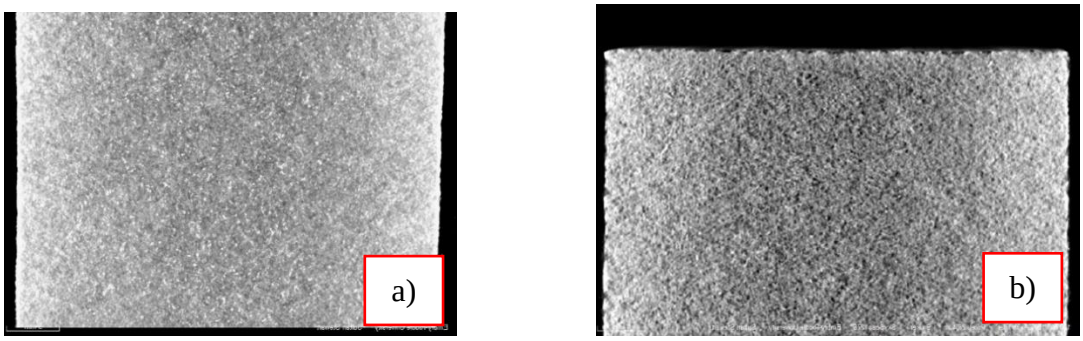

Figure 4.31 X-Ray Z-Y Plane a) Non-Infiltrated b) Silicate Submerge.

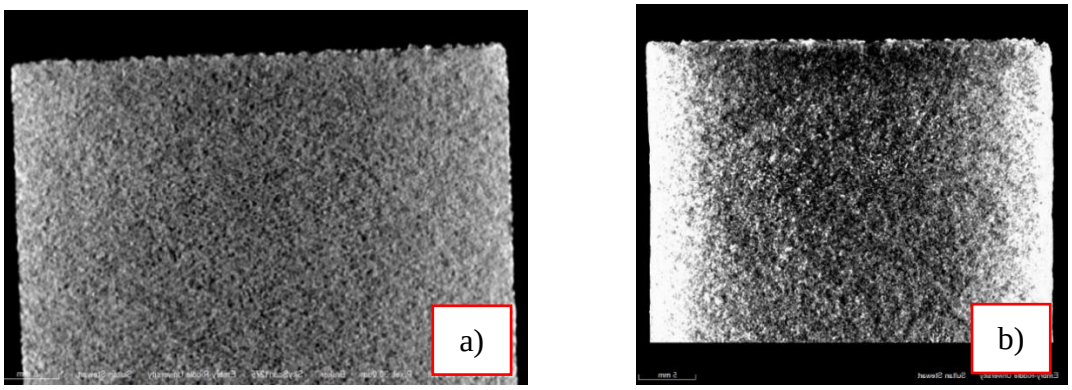

Figure 4.32 X-Ray Z-Y a) Silicate Vacuum Pull b) Zirconia Vacuum Submerge.

Cross section x-ray images of the four infiltration methods mirrors the Z-Y plane results. Similarities can be seen between the non-infiltrated, silicate – submerge and silicate – vacuum pull. The zirconia's darker areas can be attributed to the denser compaction of the zirconia particles. From SEM images, high concentration of zirconia could be seen throughout the composite's cross section which influences x-ray images.

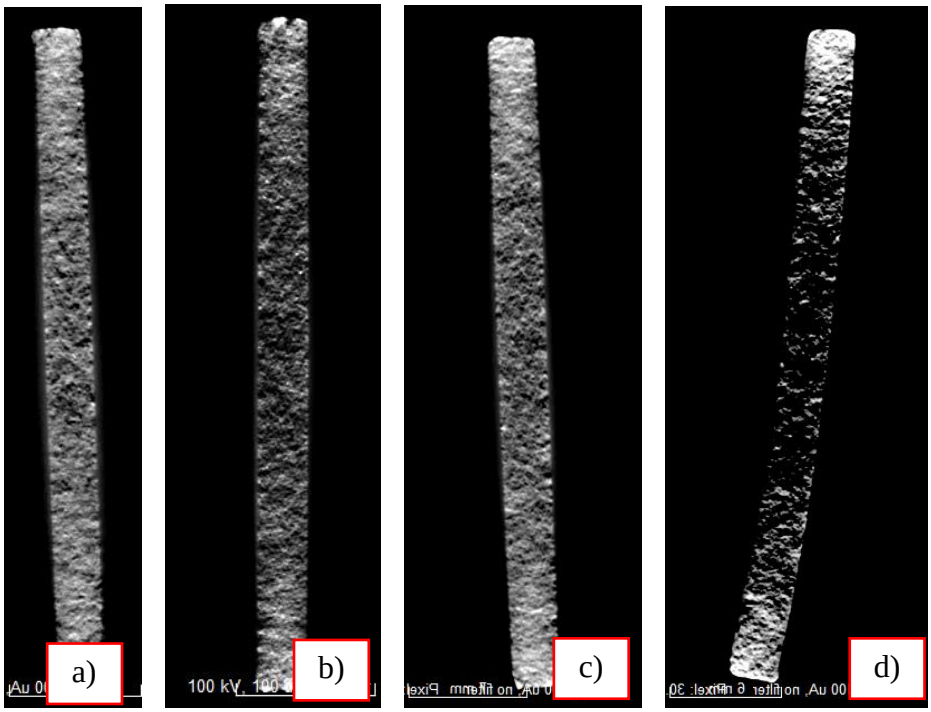

Figure 4.33 X-Ray X-Y Plane a) Non-Infiltrated b) Silicate – Submerge c) Silicate – Vacuum Pull Through d) Zirconia – Vacuum Submerge.

4.4. Hardness Testing

Hardness values were compared between composites from each infiltration method. Top and bottom sample hardness readings were taken to better determine the effect the infiltration method had on the overall hardness as well as its consistency. The average hardness of 15 HRL for the non-infiltrated scaffold was taken as the baseline for

comparison.

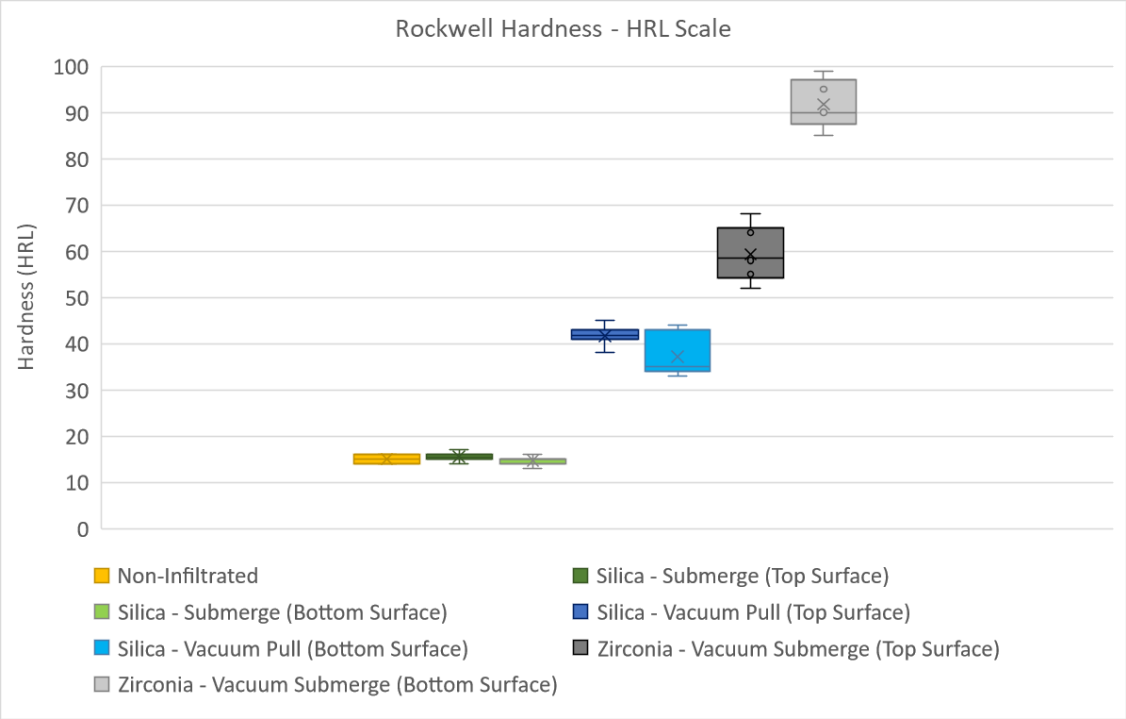

Figure 4.34 Rockwell Hardness Graph.

4.4.1. Hardness Test of Silicate – Submerge Composite

The hardness of the composites infiltrated using the silicate submerge method was nearly identical to the non-infiltrated scaffolds for both surfaces. From SEM images it was seen that a layer of the cured colloid was concentrated at the surface. It's possible that insufficient penetration throughout the sample prevented the pores from being filled by the silicate colloid to reinforce the fibers. This coupled with a relatively shallow depth of infiltration on the surface resulted in the hardness remaining unchanged.

4.4.2. Hardness Test of Silicate – Vacuum Pull Through Composite

The vacuum pull through method showed a clear increase in hardness. The top

surface had a average hardness of 42 HRL and the bottom surface had a average hardness of 37 HRL. Unlike the submerged method, it's believed that a sufficient amount of colloid infiltrated the interior of the composite. By filling the pores, the silicate reinforced the interior fibers to increase the overall hardness. The top surface hardness was more consistent than the bottom surface. This is caused by the complex pore network of the scaffold which makes infiltration difficult and increasingly inconsistent the deeper the colloid must travel.

4.4.3. Hardness Test of Zirconia – Vacuum Submerge Composite

From SEM images, the zirconia particles bonded to the Hastelloy-X fibers, reinforcing the fibers. This is evident in the increased hardness values for the zirconia – vacuum submerge method composites. The average hardness of the top surface was 59 HRL, more than three times the hardness of the non-infiltrated samples. The average hardness of the bottom surface was even higher at 92 HRL. While the zirconia hardness values are the highest, they also show the greatest variation between the top and bottom surfaces. This could be a result of the infiltration process, during the vacuum and drying steps a large amount of the zirconia eventually settled at the bottom half of the sample. If the bottom half experienced prolong exposure to the zirconia colloid perhaps infiltration was more thorough. A noticeable difference between the top and bottom surface hardness would be evident after sintering.

4.5. Nanoindentation

4.5.1. Nanoindentation Modulus Results

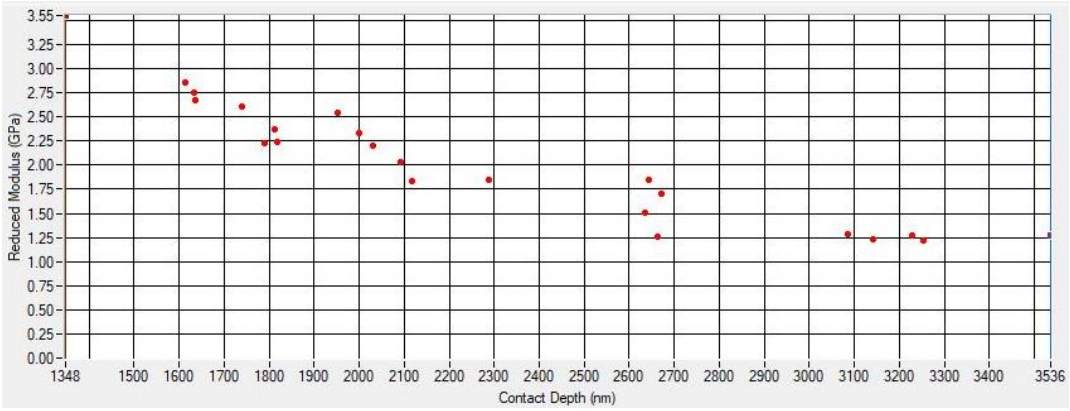

Figure 4.35 Non-Infiltrated Modulus.

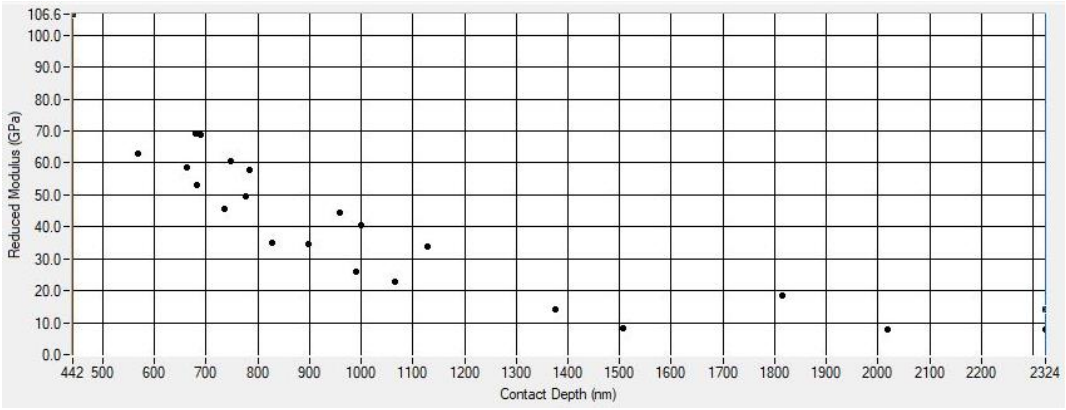

Figure 4.36 Zirconia Modulus.

Table 4.1

Nanoindentation Modulus

Composite	Mean Contact Depth (nm)	Std. Dev of Contact Depth (nm)	Mean Reduced Modulus (Gpa)	Std. Dev of Reduced Modulus (Gpa)
Non-Infiltrated	2292.835	631.943	2.03	0.637
Zirconia	1030.623	489.826	42.116	24.632

Twenty five indentations were taken with two outliers removed. In indentation data the reduced modulus is calculated considering the modulus of the sample and the indenter to account for any deformation experienced by the indenter (Rodriguez et al., 2012). Indentation instruments commonly use the Oliver-Pharr method to determine the material's reduced modulus based on the data from the indentation tests. The method starts by fitting the unloading part of the indentation load and depth data to the power law relation using equation (4.1) (Yan et al., 2012; Oliver & Pharr, 1992):

$$F = B\left(h - h_f\right)^m \tag{4.1}$$

h_f = final indentation depth after complete unloading

B and m = fitting parameters

Next, the slope of the unloading curve at the maximum indentation depth, also known as the contact stiffness (S), is calculated:

$$S = \left(\frac{df}{dh}\right)_{h=h_{max}} = Bm\left(h_{max} - h_f\right)^{m-1} \tag{4.2}$$

The contact stiffness (S) is used to estimate the contact depth (h_c) under the maximum indentation force using equation (4.3):

$$h_c = h_{max} - \epsilon \frac{F_{max}}{S} \tag{4.3}$$

ε is a constant which depends on the indenter geometry. For conical indenters a ε value of 0.72 is typically used. Afterwards, the projected contact area (A_c) for the maximum indentation force of the indenter is determined using equation (4.4):

$$A_c = \pi\left(2Rh_c - {h_c}^2\right) \tag{4.4}$$

h_c = contact depth

R = radius of the indenter tip

This is used to calculate the reduced modulus (E_r) (Yan et al., 2012; Oliver & Pharr, 1992):

$$E_r = \frac{\sqrt{\pi}}{2\beta} \frac{S}{\sqrt{A_c}} \tag{4.5}$$

β = correction factor

β accounts for the deviation in stiffness due to the lack of axis symmetry of the indenter tip. For axisymmetric indenters β is 1.0, for a square based Vickers indenter β is 1.012, and for a triangular Berkovich punch β is 1.034 (Kan et al., 2013; Oliver & Pharr, 1992). The indentation modulus is then determined using equation (4.6):

$$E_{op} = \frac{1 - {v_s}^2}{\left(\frac{1}{E_r}\right) - \left(\frac{1 - {v_i}^2}{E_i}\right)} \tag{4.6}$$

V_s = Poisson's ratio of the specimen

E_i = elastic modulus of the indenter

V_i = Poisson's ratio of the indenter

If the indenter's elastic modulus (E_i) is much larger that the tested material's elastic

modulus then the indenter can be treated as a rigid body and the indentation modulus equation (E_{op}) equation can be simplified as follows (Kan., et al 2013; Oliver & Pharr, 1992):

$$E_{op} = (1 - {v_s}^2)E_r \tag{4.7}$$

The modulus of elasticity of Hastelloy-X at room temperature in solid form is 205 – 216 Gpa. The lower reduced modulus and large range can be contributed to the varying fiber dimensions and support points. Zirconia, which has a modulus of elasticity of 97.5 – 103 Gpa, increased the reduced modulus by 20 times. Efforts were made to concentrate indentation on fibers but because the zirconia coated the fibers it's possible that some indentations were done on zirconia agglomerates which were seen in SEM images. This along with varying fiber dimensions and connection points would result in the standard deviation range seen during testing. However, even when considering the standard deviation, the reduced modulus is still well above what was measured on the non-infiltrated scaffold. It's safe to say that zirconia increased the modulus overall.

4.5.2. Nanoindentation Hardness Results

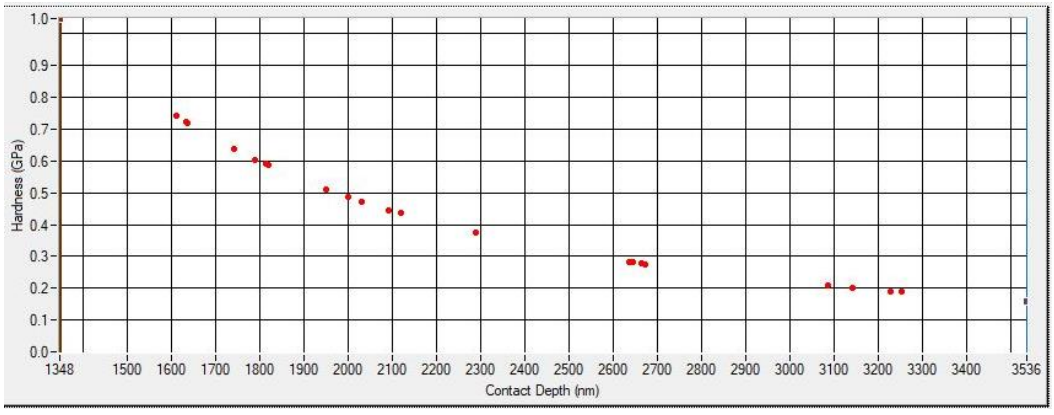

Figure 4.37 Non-Infiltrated Hardness Graph.

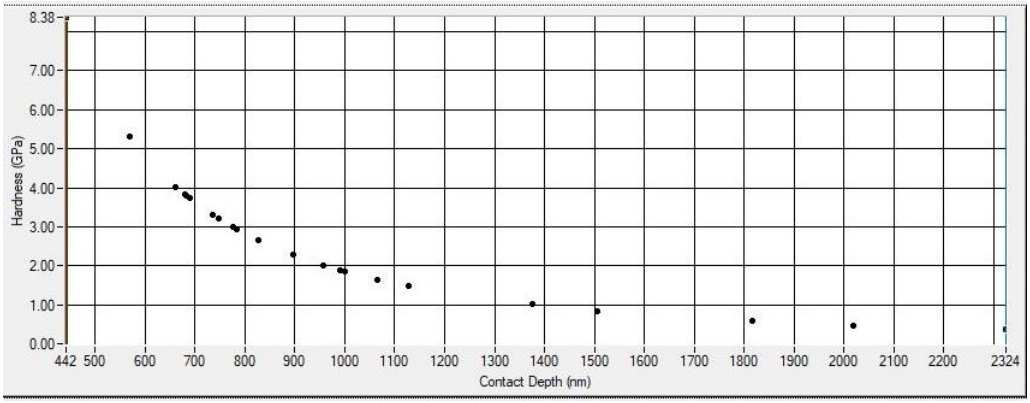

Figure 4.38 Zirconia Hardness Graph.

Table 4.2

Nanoindentation Hardness

Composite	Mean Contact Depth (nm)	Std. Dev of Contact Depth (nm)	Mean Hardness (Gpa)	Std. Dev of Hardness (Gpa)
Non-Infiltrated	2292.835	631.943	0.454	0.229
Zirconia	1030.623	489.826	2.664	1.837

Hastelloy-X has a documented hardness of 160 - 200 HV which is equivalent to a tensile strength of 510 – 640 MPa according to conversion tables (“Hardness conversion table,” n.d.). Like the modulus, the lower scaffold hardness is a result of the measurements taken on individual fibers, which don’t have the support of a solid structure. The standard deviation is large, almost half the mean hardness, caused by the random fiber dimensions, connections, and placements. Zirconia significantly influenced the overall hardness, increasing it five times compared to the non-infiltrated scaffold and

reducing the contact depth in half. This could be caused by particles restricting fiber movement during indentation. YSZ has a hardness of 259 - 287 HV which is equivalent to a tensile strength of 835 – 930 MPa according to conversion ("Hardness conversion table," n.d.). Any attempt to deform a area with a high concentration of zirconia would require more force compared to the Hastelloy-X fibers alone.

4.6. Discussion

4.6.1. Processing

When considering all the infiltration methods, porosity was only able to be reduced to a minimum of 52%. From research, thorough infiltration of scaffolds requires large pore sizes and a open network. The tortuosity of the scaffold required to minimize particle intrusion consists of various sized pores some of which were open and some closed. Consequently, this makes infiltration difficult the deeper the colloid must travel. This also explain why higher concentrations of the colloid were seen at the surface of the samples for the submerge infiltration method. Vacuum was required for infiltration to reach the interior of the scaffold but there was still a measurable difference in Rockwell hardness between the top and bottom surfaces. This indicates inconsistent infiltration across the scaffold with some pores remaining unfilled. Even so, limited infiltration might be good considering testing showed that porosities below 60% reduced the abrasion resistance of Hastelloy-X scaffolds unfavorably. ("Feltmetal^{TM}: Adaptable Abradable Materials," n.d).

4.6.2. Mechanical Behavior

Even though the zirconia composites had a higher porosity than the silicate composites, their hardness was much higher than the silicate composites. This could be related to the transformation toughening of zirconia and the difference in particle size

between the two. The smallest silicate particle size was ~2 μm whereas the zirconia particles sizes were as small as ~700 nm according to the manufacturer. Zirconia particles were able to infiltrate areas silicate particles could not, and in greater concentrations. The zirconia colloid used distilled water as the dispersion agent, drying and sintering evaporated the water leaving behind primarily zirconia which attached to the fibers of the scaffold. This is different from the silicate colloid which consists of the silicate particles within a resin which does not evaporate during curing. Perhaps if after curing, solely silicate was left the hardness values would be greater.

In recent years, scratch testing has been investigated specifically as a option for measuring abrasion resistance in turbine engine applications. It is simpler, quicker and more cost effective then developing a apparatus to mimic the highspeed turbine blade application. While research has limited this testing primarily to abradable coatings, scratch testing was performed on the scaffolds to determine abrasion resistance. Unfortunately, for this thesis the results were not definitive due to the high porosity and large pore sizes in the scaffold.

However, there is research to correlate some material properties to scratch testing. It was determined that a major contributor to reduced abradability is plastic deformation. High hardness and elastic modulus resulted in greater densification of the surrounding material during deformation by scratch testing. This required a greater compressive force by the scratch indenter therefore reducing the abradability. To increase abradability higher fracture is needed to avoid densification. It is worth noting that in the study by Ma and Matthews, the samples with the highest porosity were less abradable then the samples with the lowest porosity (Ma & Matthews, 2007).

Scratch testing requires compression of the indenter, that compression influences the abradability. As compression force increases it reasonable to assume that abradability would decrease. Non-infiltrated scaffolds would theoretically require a lower compression force then the silicate or zirconia composites. If a load is applied on a fiber that is fixed at each end, Figure 4.39, a force can be determined.

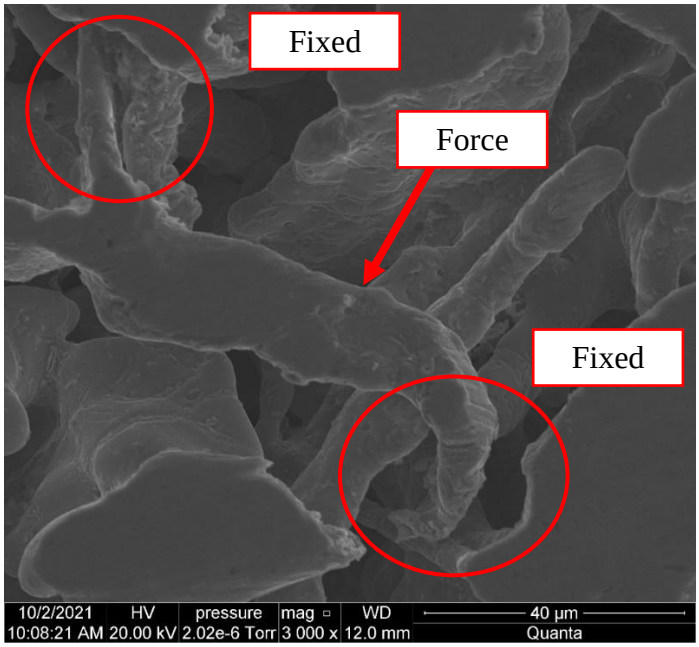

Figure 4.39 Non-Infiltrated - Cross Section 3,000CAPX.

If this same loading scenario is applied to the silicate or zirconia composite, the force required for deformation would be greater than the non-infiltrated samples. This is because at least one end of the fiber is reinforced, shortening the free length of the fiber, Figure 4.40. The same can be said about the zirconia composite, in Figure 4.41 the entire length of the fiber is supported by the zirconia. This would require a even greater compression force to deform. Therefore, it is reasonable to assume that the non-infiltrated

scaffold would have better abradability compared to the silicate and zirconia composites.

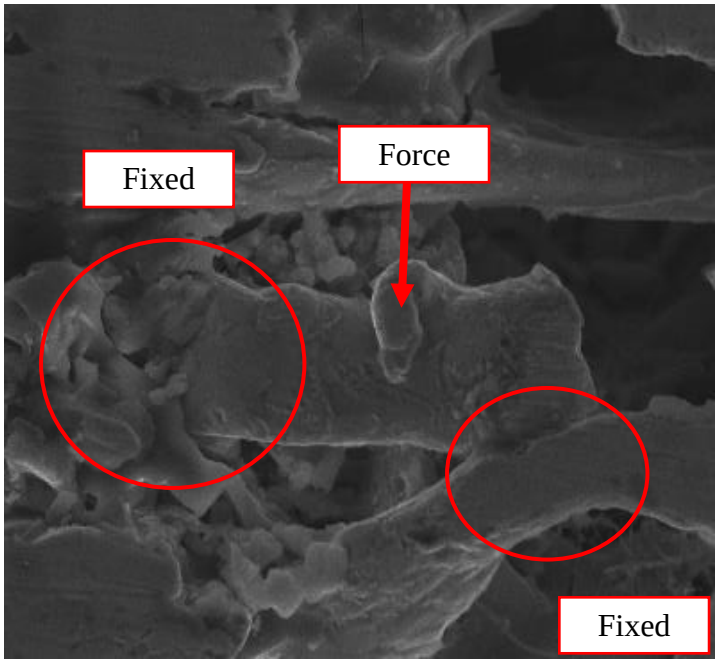

Figure 4.40 Silicate - Submerge - Top Surface 1,750CAPX.

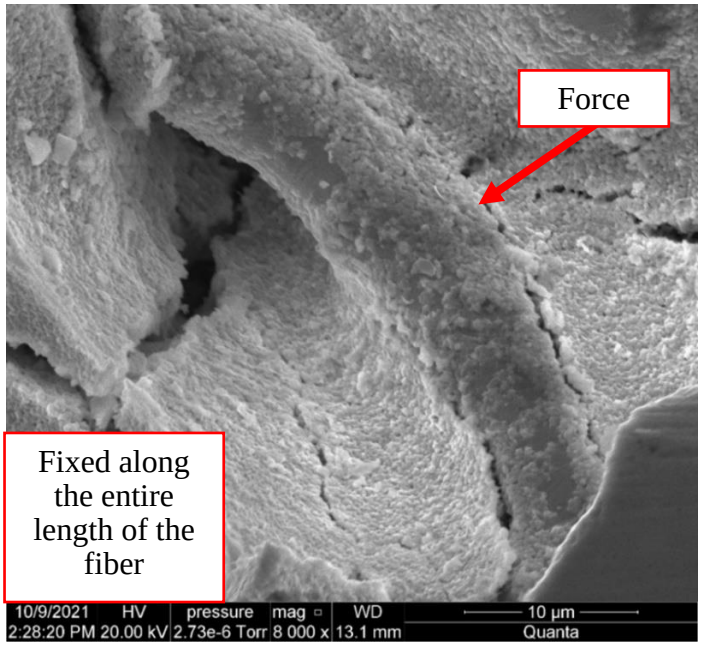

Figure 4.41 Zirconia - Cross Section 8,000CAPX.

5. Conclusions and Future Work

Hastelloy-X alloy scaffolds with 80% porosity were infiltrated with a room temperature curing silicate colloid and a novel zirconia colloid. Various fabrication processes, some using vacuum and pressure were utilized to infiltrate the scaffold. Scaffolds were ultimately sintered to form metal matrix composites. The composites were characterized using x-ray tomography and SEM imaging to analyze the pore infiltration. Rockwell hardness and nanoindentation were measured to determine changes in material properties.

5.1. Conclusions

It was determined from SEM imaging and hardness tests that the most effective infiltration methods required vacuum. For the silicate colloid the vacuum pull through method was the most effective. The pores that were infiltrated were filled with the silicate particles and cured colloid. The vacuum submerge method was sufficient for the zirconia colloid. Once sintered, infiltrated pores consisted of Hastelloy-X fibers coated with zirconia particles with some agglomerates present. Overall, limited porosity was achieved due to the complex pore network of the scaffold. This complexity that is meant to minimize particle intrusion also limited colloid infiltration, resulting in limited porosity reductions. The smaller zirconia particle size and use of a evaporating dispersion media (distilled water) resulted in a high concentration of zirconia in the pores. As a result, the zirconia composite hardness was higher despite having greater porosity than the silicate composites.

5.2. Future Work

To further evaluate the material properties mechanical testing will be necessary. Nano

indentation test for the silicate composites should be conducted along with high temperature nano indentation to determine how the composites preform at elevate temperatures. Wear testing will better identify how the composites perform against high velocity particulate erosion. Fracture test will determine if ceramic aids in the composite's ability to break away when contacted by a high-speed rotating blade instead of deforming. Also, research regarding how varying porosity levels affect the material properties could be beneficial in optimizing material performance.

Modeling should be attempted to better understand the pore network of scaffolds made by sintering fibers. This will help explain why infiltration is limited and what can be done to create a more open pore network susceptible to infiltration.

REFERENCES

Akash Saxena, Neera Singh, Devendra Kumar, Pallav Gupta. (2017). Effect of Ceramic Reinforcement on the Properties of Metal Matrix Nanocomposites. *Materials Today: Proceedings*, *4*(4E), 5561–5570. https://doi.org/10.1016/j.matpr.2017.06.013

Almotairy, S., Boostani, A., Hassani, M., Wei, D., Jiang, Z. (2020). Effect of hot isostatic pressing on the mechanical properties of aluminium metal matrix nanocomposites produced by dual speed ball milling. *Journal of Materials Research and Technology*, *9*(2), 1151-1161. https://doi.org/10.1016/j.jmrt.2019.11.043

Amat, N., Muchtar, A., Ghazali, M., Yahaya, N. (2013). Suspension stability and sintering influence on yttria-stabilized zirconia fabricated by colloidal processing. Ceramics International, *40*(4), 5413-5419. https://doi.org/10.1016/j.ceramint.2013.10.123

ANSYS. (2020). Granta EduPack [computer software]. Pennsylvania: Canonsburg.

ASTM Designation E18-15 Standard Test Methods for Rockwell Hardness of Metallic Materials [PDF file]. (2018). Retrieved September 18 from https://repositorio.uisek.edu.ec/bitstream/123456789/2680/3/ASTM_E18-15.pdf

Attar, H., Bonisch, M., Calin, M., Zhang, L., Scudino, S., Eckert, J. (2014). Selective laser melting of in situ titanium–titanium boride composites: Processing, microstructure and mechanical properties. *Acta Materialia*, *76*, 13-22. https://doi.org/10.1016/j.actamat.2014.05.022

Bergstrom, L. (2001). Chapter 9 Colloid Processing of Ceramics. In K. Holmberg (Ed.). *Handbook of Applied Surface and Colloid Chemistry*. (pp. 201-217). New York, NY: John Wiley & Sons, Ltd.

Bommala, V., Krishna, M., Rao, C. (2019). Magnesium matrix composites for biomedical applications: A review. *Journal of Magnesium and Alloys*, *7*(1), 72–79. https://doi.org/10.1016/j.jma.2018.11.001

Boppana, S., Dayanand, S., Kumar, A., MR, Kumar, V., Aravinda T. (2020). Synthesis and characterization of nano graphene and ZrO_2 reinforced Al 6061 metal matrix composites. *Journal of Materials Research and Technology*, *9*(4), 7354-7362. https://doi.org/10.1016/j.jmrt.2020.05.013

Bostani, B., Ahmadi, N., Yazdani, S. (2016). Manufacturing of functionally graded Ni–ZrO_2 composite coating controlled by stirring rate of the electroplating bath. *Surface Engineering*, *32*(7), 495-500. https://doi.org/10.1080/02670844.2016.1148307

Bull, S. (1999). Can scratch testing be used as a model for the abrasive wear of hard coatings? *Wear*, 233–235 & 412–423. https://doi.org/10.1016/S0043-1648(99)00207-0

Capillary-active impregnation and sealing with dichtol of DIAMANT®. (n.d.). Retrieved from https://www.diamant-polymer.de/en/products/dichtol/

Deb, P., Sarker, P., Barbhuiya, S. (2015). Effects of nano-silicate on the strength development of geopolymer cured at room temperature. *Construction and Building Materials 101*, 675-683. https://doi.org/10.1016/j.conbuildmat.2015.10.044

Dey, A., Pandey, K. (2016). Characterization of Fly Ash and Its Reinforcement Effect on Metal Matric Composites: A Review. *Review of Advance Material Science, 44*, 168-181. Retrieved from https://www.ipme.ru/e-journals/RAMS/no_24416/05_24416_dey.pdf

Dichtol HTWG Hydro Product number #2506 F047/2017 [PDF file]. (2018). Retrieved October 8, 2021 from https://www.diamant-polymer.de/wp-content/uploads/dichtol-HTWG-Hydro-2506-EN.pdf

Dmitruk, A., Zak, A., Naplocha, K., Dudzinski, W., Morgiel, J. (2018). Development of pore-free Ti-Al-C MAX/Al-Si MMC composite materials manufactured by squeeze casting infiltration. *Materials Characterization, 146*, 182–188. https://doi.org/10.1016/j.matchar.2018.10.005

Dourandish, M., Simchi, A., Shabestary, E., Hartwigz, T. (2008). Pressureless Sintering of 3Y-TZP/Stainless-Steel Composite Layers. *Journal of the American Ceramic Society, 91*(11), 3493–3503. https://doi.org/10.1111/j.1551-2916.2008.02658.x

El-Galy, I., Ahmed, M., Bassiouny, B. (2017). Characterization of functionally graded Al-SiCp metal matrix composites manufactured by centrifugal casting. *Alexandria Engineering Journal, 56*(4), 371-381. https://doi.org/10.1016/j.aej.2017.03.009

Feltmetal ™ Abradable Seals [Company Website]. (n.d.). Retrieved June 26, 2021 from https://technetics.com/products/feltmetal-abradable-seals/

Garvie, R., Hannink, R., Pascoe, R. (1990). Ceramic steel? *Sintering Key Papers*, 253-257.

Gomes, O., Teixeira, F., Lima, J., Silva, F. (2018). On the measurement of cross-sectional area of natural fibers. *4th Brazilian Conference on Composite Materials*. https://doi.org/10.21452/bccm4.2018.10.10

Gonzalo-Juan, I., Ferrari, B., Colomer, M. Sánchez-Herencia, A.J. (2010). Colloid processing and sintering of porous percolative Ni-YSZ layers. *Journal of Membrane Science, 352*(1-2), 55-62. https://doi.org/10.1016/j.memsci.2010.01.060

Haghighi, R., Jahromi, S., Moresedgh, A., Jhorshid, M. (2012). A Comparison Between ECAP and Conventional Extrusion for Consolidation of Aluminum Metal Matrix Composite. *Journal of Material Engineering and Performance, 21,* 1885–1892. Retrieved from https://link.springer.com/article/10.1007/s11665-011-0108-9

Hardness conversion table - Tensile strength, Vickers, Brinell OCH Rockwell. (n.d.) Retrieved September 18, 2021 from https://www.bbshalmstad.se/en/infocenter/hardness-conversion-table

Hastelloy® X alloy. (n.d.). Retrieved September 18, 2021 from https://www.haynesintl.com/alloys/alloy-portfolio_/High-temperature-Alloys/HASTELLOY-X-alloy/HASTELLOY-X-principal-features.aspx

Hehr, A., Wenning, J., Norfolk, M., Sheridan, J., Newman, J., Domack, M. (2019). Selective Reinforcement of Aerospace Structures Using Ultrasonic Additive Manufacturing. *Journal of Materials Engineering and Performance, 28,* 633–640. Retrieved from https://link.springer.com/article/10.1007/s11665-018-3614-1

Hoa, S., Hutmachera. D. (2005). A comparison of micro CT with other techniques used in the characterization of scaffolds. *Biomaterials, 27*(8), 1362–1376. https://doi.org/10.1016/j.biomaterials.2005.08.035

Imran, M., Anwar Khan, A. (2019). Characterization of Al-7075 metal matrix composites: a review. *Journal of Materials Research and Technology, 8*(3), 3347-3356. https://doi.org/10.1016/j.jmrt.2017.10.012

Jing, Z., Dejun, K. (2018). Effect of laser remelting on friction-wear behaviors of cold sprayed Al coatings in 3.5% NaCl solution. *Materials, 11*(283), 1-14. https://doi.org/10.3390/ma11020283

Kan, Q., Yan, W., Kang, G., Sun, Q. (2013). Oliver–Pharr indentation method in determining elastic moduli of shape memory alloys—A phase transformable material. *Journal of the Mechanics and Physics of Solids, 61*(10), 2015–2033. https://doi.org/10.1016/j.jmps.2013.05.007

King, D., Henfling, J. (2013). Evaluation of Thermal Spray Coatings and Shape Memory Alloys as Pressure Seals for Downhole Tools. Retrieved from https://www.osti.gov/servlets/purl/1079016

Kolnes, M., Kubarsepp, J., Sergejev, F., Kolnes, M., Tarraste, M., Viljus, M. (2020). Performance of Ceramic-Metal Composites as Potential Tool Materials for Friction Stir Welding of Aluminium, Copper and Stainless Steel. *Materials, 13*(8). Retrieved from https://www.mdpi.com/1996-1944/13/8/1994

Lee, C., Li, H., Chandel, R. (1999). Vacuum-free diffusion bonding of aluminium metal matrix composite. *Journal of Materials Processing Technology*, 89-90 & 326-330. https://doi.org/10.1016/S0924-0136(99)00144-2

Lukacs III, A. (2006). Polysilazane Precursors to Advanced Ceramics. *American Ceramic Society Bulletin, 86*(1). Retrieved from https://www.coursehero.com/file/40025664/Lukacspdf/

Ma, X., Matthews. A. (2007). Investigation of abradable seal coating performance using scratch testing. *Surface & Coatings Technology, 202*(4-7), 1214–1220. https://doi.org/10.1016/j.surfcoat.2007.07.076

Mattern, A., Huchler, B., Staudenecker, D., Oberacker, R., Nagel, A., Hoffmann, M.J. (2004). Preparation of interpenetrating ceramic–metal composites. *Journal of the European Ceramic Society, 24*, 3399–3408. https://doi:10.1016/j.jeurceramsoc.2003.10.030

Miracle, D. (2005). Metal matrix composites – From science to technological significance. *Composites Science and Technology, 65*(15-16) 2526–2540. https://doi.org/10.1016/j.compscitech.2005.05.027

Molin, S., Tolczyk, M., Gazda, M., Jasinski, P. (2011). Stainless Steel/Yttria Stabilized Zirconia Composite Supported Solid Oxide Fuel Cell. *Journal of Fuel Cell Science and Technology, 8*(051019), 1-4.

Oliver, W., Pharr, G. (1992). An improved technique for determining hardness and elastic modulus using load and displacement sensing indentation experiments. *Journal of Material Research 7*(6), 1564-1583. Retrieved from https://web.mit.edu/cortiz/www/3.052/3.052CourseReader/45_OliverPharr1992Nanoindentation.pdf

Ordoneza, F., Chejnec, F., Pabon, E., Cacua, K. (2020). Synthesis of ZrO_2 nanoparticles and effect of surfactant on dispersion and stability. *Ceramics International 46*(8), 11970–11977. https://doi.org/10.1016/j.ceramint.2020.01.236

Ormer, H. (n.d.). Utilizing Venturi Vacuum Generators Efficiently. Blower & Vacuum Best Practices. Retrieved November 13, 2021 from https://www.blowervacuumbestpractices.com/system-assessments/vacuum-generation/utilizing-venturi-vacuum-generators-efficiently

Pandey, U., Purohit, R., Agarwal P., Singh, S. (2018). Study of Fabrication, Testing and Characterization of Al/TiC Metal Matrix Composites through different Processing Techniques. *Materials Today: Proceedings, 5*, 4106–4117. https://doi.org/10.1016/j.matpr.2017.11.671

Philips, K., Azar M., Montalbano, T., VaBen, R., Mumm, D. (2016). Abradable Sealing Materials for Emerging IGCC-Based Turbine Systems [PowerPoint slides]. Retrieved July 3, 2021 from https://netl.doe.gov/sites/default/files/event-proceedings/2016/utsr/Wednesday/Daniel-Mumm.pdf

Piconi, C., Maccauro, G. (1997). Review Zirconia as a ceramic biomaterial. *Biomaterials, 20*, 1-25. Retrieved from https://pubmed.ncbi.nlm.nih.gov/9916767/

Poria, S., Sahoo, P., Sutradhar, G. (2016). Tribological Characterization of Stir-cast Aluminium-TiB2 Metal Matrix Composites. *Silicon, 8*, 591–599. https://doi.org/10.1007/s12633-016-9437-5

Prashanth, K., Scudino, S., Chaubey, A., Lober, L., Wang, P., Attar, H., Schimansky, F., Pyczak, F., Eckert, J. (2016). Processing of Al–12Si–TNM composites by selective laser melting and evaluation of compressive and wear properties. *Journal of Material Research, 31*(1). https://doi.org/10.1557/jmr.2015.326

Product Specification Zirconia(IV) oxide-yttria stabilized PRD.2.ZQ5.10000031753 [PDF file]. (n.d.). Retrieved from https://www.sigmaaldrich.com/specification-sheets/534/464/464228-BULK_____ALDRICH__.pdf

Raj, R. (2018). Introducing Nanoscale Ceramic Particles into Metal Matrices. *Advanced Materials & Processes, 176*(3). Retrieved from https://go.gale.com/ps/i.do?id=GALE%7CA539811079&sid=googleScholar&v=2.1&it=r&linkaccess=abs&issn=08827958&p=AONE&sw=w&userGroupName=anon%7E892c00f9

Rami, M., Meireles, M., Cabane, B., Guizard, C. (2009). Colloidal Stability for Concentrated Zirconia Aqueous Suspensions. *Journal of American Ceramic Society, 92*(S1) S50-S56. https://doi.org/10.1111/j.1551-2916.2008.02681.x

Rawal, S. (2001). Metal-Matrix Composites for Space Applications. MMCs for Space Overview *JOM*, 14-17. Retrieved from https://link.springer.com/content/pdf/10.1007/s11837-001-0139-z.pdf

Rodriguez, S., Alcala, J., Souza, R., (2012). The reduced modulus in the analysis of sharp instrumented indentation tests. *Journal of Material Research, 27*(16). https://doi.org/10.1557/jmr.2012.164

Saxenaa, A., Singh, N., Kumara, D., Gupta, P. (2017). Effect of Ceramic Reinforcement on the Properties of Metal Matrix Nanocomposites. *Materials Today: Proceedings, 4*(4), 5561–5570. https://doi.org/10.1016/j.matpr.2017.06.013

Scherma, F., Volkl, R., Smaalen, S., Mondal, S., Plamondon, P., Esperance, G., Bechmann, F., Glatzel, U. (2009). Microstructural characterization of interpenetrating light weight metal matrix composites. *Materials Science and Engineering: A, 518*(1-2), 118–123. https://doi.org/10.1016/j.msea.2009.04.010

Singer, A. (1991). Metal matrix composites made by spray forming. *Materials Science and Engineering: A*, 135, 13-17. https://doi.org/10.1016/0921-5093(91)90528-U

Singerman, S., Jackson., J. (1996). Titanium Metal Matrix Composites for Aerospace Applications. *The Minerals, Metals & Materials Society*, 579-586. Retrieved from https://www.tms.org/superalloys/10.7449/1996/superalloys_1996_579_586.pdf

Singh, N., Mazumder, R., Gupta, P., Kumar, D. (2017). Ceramic Matrix Composites: Processing Techniques and Recent advancements. *Journal of Materials and Environmental Sciences 8*(5), 1654-1660. Retrieved from https://www.jmaterenvironsci.com/Document/vol8/vol8_N5/176-JMES-2775-Singh.pdf

Sofianos, M., Chaudhary, A., Paskevicius, M., Sheppard, D., Humphries, T., Dornheim, M., Buckley. C. (2018). Hydrogen storage properties of eutectic metal borohydrides melt-infiltrated into porous Al scaffolds. *Journal of Alloys and Compounds*, *775, 474-480*. https://doi.org/10.1016/j.jallcom.2018.10.086

Sofianos, M., Sheppard, D., Rowles, M., Humphries, T., Liu, S., Buckley, C. (2017). Novel synthesis of porous Mg scaffold as a reactive containment vessel for $LiBH_4$. *The Royal Society of Chemistry Advances, 7*, 36340-36350. https://doi.org/10.1039/C7RA05275H

Stringer, J., Marshall, M. (2012). High speed wear testing of an abradable coating. *Wear*, 294–295, 257–263. https://doi.org/10.1016/j.wear.2012.07.009

SZ0429 Yttria Stabilized Zirconia Y2O3·ZrO2 (YSZ). (n.d.). Retrieved November 6, 2021 from https://www.samaterials.com/zirconium/429-yttria-stabilized-zirconia.html

Tarabay, J., Peres, V., Serris, E., Valdivieso, F., Pijolat, M. (2012). Zirconia matrix composite dispersed with stainless steel particles: Processing and oxidation behavior. *Journal of the European Ceramic Society, 33*(6), 1101-1110. https://doi.org/10.1016/j.jeurceramsoc.2012.11.020

Technetics Group. *Feltmetal™: Adaptable Abradable Materials*. Deland, FL.

Technical Data Zirconia (Zirconium Oxide, ZrO_2). (n.d.). Retrieved October 30, 2021 from https://global.kyocera.com/prdct/fc/list/material/zirconia/zirconia.html

Thermal spray coatings: impregnation and sealing. (n.d.). Retrieved August 7, 2021 from https://www.diamant-polymer.de/en/products/dichtol/thermal-spray-coatings/

Transformation toughening of YTZP: How it Resists Crack Propagation [PDF file]. (n.d.). Retrieved November 6, 2021 from https://www.ceramics.net/sites/default/files/stc-white-paper-ytzp-yttria-stabilized-zirconia-low-transformation-toughening-01062021.pdf

Vasylkiv, O., Sakka, Y. (2001). Synthesis and Colloidal Processing of Zirconia Nanopowder. *Journal of American Ceramic Society, 84*(11) 2489-2494. https://doi.org/10.1111/j.1151-2916.2001.tb01041.x

Yan, W., Pun, C., Simon, G. (2012). Conditions of applying Oliver–Pharr method to the nanoindentation of particles in composites. *Composites Science and Technology, 72*(10), 1147–1152. https://doi.org/10.1016/j.compscitech.2012.03.019

Yttria Stabilized Zirconia, YSZ. MatWeb Material Property Data. (n.d.). Retrieved November, 6, 2021 from http://www.matweb.com/search/datasheet.aspx?matguid=4e3988dd9adb4d1ca37a1b2cbab87d9a&ckck=1

Yttria Stabilized Zirconia, YSZ (ZrO2 / Y2O3) Nanoparticles. (2013). Retrieved September 18, 2021 from https://www.azonano.com/article.aspx?ArticleID=3374

Zhang, J., Kong, D. (2018). Effect of laser remelting on microstructure and immersion corrosion of cold–sprayed aluminum coating on S355 structural steel. *Optics & Laser Technology, 106*, 348-356. https://doi.org/10.1016/j.optlastec.2018.04.026

Zhang, J., Kong, D. (2018). Microstructures and salt spray corrosion behaviors of cold sprayed Al coatings on S355 steel in marine environment. *Surface Review and Letters, 2*5(6). https://doi.org/10.1142/S0218625X18501159

Zhao, X., Gu, D., Ma, C., Xi, L., Zhang, H. (2019). Microstructure characteristics and its formation mechanism of selective laser melting SiC reinforced Al-based composites. *Vacuum, 160*, 189-196. https://doi.org/10.1016/j.vacuum.2018.11.022

Zirconia(IV) oxide-yttria stabilized. (n.d.). Retrieved June 19, 2021 from https://www.sigmaaldrich.com/US/en/product/aldrich/464228?cm_sp=Insite-_-caContent_prodMerch_gruCrossEntropy-_-prodMerch10-1

Zirconia(IV) oxide-yttria stabilized. SDS No. 464228 [PDF file]. (2021). Retrieved October 8, 2021 from https://www.sigmaaldrich.com/US/en/sds/aldrich/464228